Article:
Atkins, AL, Shaw, S and Peacock, CL (2016) Release of Ni from birnessite during transformation of birnessite to todorokite: Implications for Ni cycling in marine sediments. Geochimica et Cosmochimica Acta, 189. pp. 158-183. ISSN 0016-7037

https://doi.org/10.1016/j.gca.2016.06.007

*Manuscript

Release of Ni from birnessite during transformation of birnessite to todorokite: Implications for Ni cycling in marine sediments

Amy L. Atkins[1§], Samuel Shaw[2] and Caroline L. Peacock[1]*

[1]University of Leeds, School of Earth and Environment, Leeds, LS2 9JT, UK.

[2]University of Manchester, School of Earth, Atmospheric and Environmental Sciences, Manchester, M13 9PL, UK.

[§]Current address: ETH Zürich, Department of Environmental Systems Science, Institute of Biogeochemistry and Pollutant Dynamics, Soil Chemistry Group, Universitätstrasse 16 CH-8092 Zürich, Switzerland.

Submitted to Geochimica et Cosmochimica Acta

Date 22 July 2015

Revised version submitted 11th May 2016

*Corresponding author e-mail: C.L.Peacock@leeds.ac.uk

ABSTRACT

The phyllomanganate birnessite is the main Mn-bearing phase in oxic marine sediments where it exerts a primary control on the concentration of micronutrient trace metals in seawater. However, during sediment diagenesis and under mild hydrothermal conditions birnessite transforms into the tectomanganate todorokite. We have recently shown that the transformation of birnessite to todorokite proceeds via a four-stage nucleation and growth mechanism, beginning with todorokite nucleation, then crystal growth from solution to form todorokite primary particles, followed by their self-assembly and oriented growth via oriented attachment to form crystalline todorokite laths, culminating in traditional crystal ripening (Atkins et al., 2014, GCA 144, 109-125). Here we determine the fate and mobility of Ni sorbed by birnessite during this transformation process. Specifically, in our recent work we predict that the presence of Ni within the phyllomanganate matrix will disrupt the formation of todorokite primary particles. As such, contrary to current understanding, we suggest that Ni sorbed by birnessite will slow the transformation of birnessite to todorokite and/or be released to marine porewaters during sediment diagenesis. Here we transform a synthetic, poorly crystalline, Ni-sorbed (~1 wt% Ni) hexagonal birnessite, analogous to marine birnessite, into todorokite under a mild reflux procedure, developed to mimic marine diagenesis and mild hydrothermal conditions. We characterize our birnessite and reflux products as a time series, including X-ray diffraction (XRD), high-resolution transmission electron microscopy (HR-TEM) and extended X-ray absorption fine structure (EXAFS) spectroscopy. In addition we determine Ni speciation and mineral phase associations in a suite of natural marine ferromanganese precipitates, containing intermixed phyllomanganate and todorokite. Our work shows for the first time that Ni significantly slows the transformation of birnessite to todorokite and reduces the crystallinity of the neo-formed todorokite phase, but does not alter the mechanism and pathway of todorokite formation, compared to a Ni-free system. Furthermore, in systems tending towards todorokite as the final diagenetic product, we see that up to 50 % of the Ni originally sequestered by birnessite is released to solution during the transformation. Our work indicates that the transformation of birnessite to todorokite in oxic marine sediments likely provides a significant source of Ni to marine sedimentary porewaters and potentially a hitherto unrecognized benthic flux of Ni to seawater.

KEYWORDS: vernadite, birnessite, buserite, todorokite, nickel, manganese oxide, ferromanganese, transformation, oriented aggregation, seawater.

1. INTRODUCTION

The phyllomanganates birnessite and buserite, together with the tectomanganate todorokite, are the dominant Mn-bearing minerals in oxic marine sediments and ferromanganese deposits, where they are typically found as poorly crystalline and intermixed nanoparticulate phases (e.g., Goldberg, 1954; Burns and Burns, 1977; Usui and Terashima, 1997; Banerjee et al., 1999; Post, 1999). Birnessite and buserite in particular are highly reactive and through coupled sorption and redox reactions exert a strong control on the concentration, speciation and bioavailability of trace metals and micronutrients in seawater (e.g., Post, 1999). Indeed, the poorly crystalline phyllomanganates present in ferromanganese crusts and nodules are typically enriched in trace metals such as Ni, Cu and Zn by ~10^6 over their respective concentrations in seawater (e.g., Arrhenius, 1963; Koschinsky and Hein, 2003). Specifically with regard to Ni, ferromanganese oxides dispersed in pelagic sediments and precipitated as discrete crusts and nodules provide the only known sinks for Ni in the modern marine Ni cycle (Gall et al., 2013). These minerals typically contain between ~0.2-1 bulk wt% Ni, exclusively sorbed to the Mn-rich fraction (e.g., Koschinsky and Halbach, 1995; Koschinsky and Hein, 2003; Peacock and Sherman, 2007a), as a result of a sorption equilibrium between Ni and poorly crystalline phyllomanganate that is predicted to provide a primary control on the concentration of Ni in the modern oceans (Peacock and Sherman, 2007b).

In oxic marine sediments however, the poorly crystalline phyllomanganates transform into todorokite during oxic diagenesis and under mild hydrothermal conditions. In the case of Ni, previous work shows that dissolved Ni is readily sequestered to birnessite via surface complexation above and below Mn octahedral vacancy sites present on the birnessite [001] surface (space group p63/mmc) (e.g., Manceau et al., 2007a,b; Peacock and Sherman, 2007a,b; Peacock, 2009; Peña et al., 2010). Subsequent to this initial sequestration, with aging and under pH conditions relevant to the marine environment, surface complexed Ni progressively migrates into the birnessite crystal lattice to become structurally incorporated (Peacock, 2009), and in natural marine ferromanganese precipitates Ni is found entirely incorporated into birnessite and buserite (Peacock and Sherman, 2007a). Despite our understanding of Ni sequestration by phyllomanganates, the mobility and fate of Ni and other micronutrients during the transformation of these phases into todorokite remains unclear. Our recent work on the mechanism of todorokite nucleation and growth suggests that, contrary to current understanding, trace metals like Ni might slow the transformation of birnessite to

88 todorokite and be released to marine sedimentary porewaters during this diagenetic
89 process, thus potentially providing a benthic flux of these micronutrients to seawater
90 (Atkins et al., 2014). A complete knowledge of the controls on Ni concentrations and
91 isotopic compositions in seawater is important for our understanding of the modern
92 marine Ni cycle (e.g., Cameron and Vance, 2014), and also for the interpretation of palaeo
93 Ni signals recorded in marine sedimentary archives (e.g., Cameron et al., 2009; Konhauser
94 et al., 2009).

95 In the natural environment Mn(III/IV) oxides are thought to form via the microbial
96 oxidation of Mn(II) (e.g., Brouwers, 2000; Francis et al., 2001; Bargar et al., 2000, 2005;
97 Villalobos et al., 2003; Tebo et al., 2005; Webb et al., 2005a, b; Saratovsky et al., 2006;
98 Spiro et al., 2010). However, although todorokite is often found intimitely associated with
99 turbostratic phyllomanganate (termed vernadite) and both 7 Å (birnessite) and 10 Å
100 (buserite) semi-coherently stacked phyllomanganates (here all collectively termed poorly
101 crystalline phyllomanganates) in marine ferromanganese precipitates (e.g., Burns and
102 Burns, 1978a, b; Siegel and Turner, 1983; Usui and Terashima, 1997; Banerjee et al.,
103 1999; Bodeï et al., 2007; Peacock and Moon, 2012), it is thought to only form during the
104 transformation of a phyllomanganate during oxic sediment diagenesis and under low
105 temperature hydrothermal conditions (e.g., Burns and Burns, 1978b). Indeed,
106 observations from both natural ferromanganese samples and experiments largely support
107 this assertion. For example, todorokite is rarely found in hydrogenetic ferromanganese
108 crusts precipitated directly from ambient seawater, but is found to varying extents in
109 diagenetic ferromanganese nodules formed at the sediment-seawater interface with
110 influence from sediment porewaters, and is prevalent in hydrothermal ferromanganese
111 deposits formed in close proximity to hydrothermal fluids (e.g., Burns and Burns, 1977).
112 Moreover, all todorokite synthesis procedures to date involve the transformation of a
113 phyllomanganate via either a high temperature and pressure hydrothermal treatment (e.g.,
114 Giovanoli et al., 1975; Golden et al., 1987; Shen et al., 1993; Feng et al., 1995, 1998; Tian
115 et al., 1997; Vileno et al., 1998; Ching et al., 1999; Luo et al., 1999; Malinger et al., 2004;
116 Liu et al., 2005) or a more mild refluxing process at atmospheric pressure, designed to
117 better simulate todorokite formation in natural environments (e.g., Feng et al., 2004, 2010;
118 Cui et al., 2006, 2008, 2009; Atkins at al., 2014). To best replicate the morphological and
119 structural features of natural marine todorokite, these syntheses are typically performed in
120 a Mg-rich electrolyte (~1 M $MgCl_2$) where Mg is prevalent in marine sediment porewaters
121 and acts as a templating ion, expanding the precursor birnessite interlayers from ~7 Å to

~10 Å (e.g., Bodeï et al., 2007), which closely matches the eventual tunnel dimensions of the neo-forming todorokite (where ideal todorokite consists of triple chains of edge-sharing MnO_6 octahedra that share corners to form 3D tunnels equating to ~10x10 Å (Burns et al., 1985; Post and Bish, 1988; Post et al., 2003)). Attempts to synthesise todorokite using Ca as a templating ion (likely more relevant to terrestrial todorokite) typically result in an incomplete transformation (e.g., Golden et al., 1987) and may in part explain the relative rarity of todorokite in terrestrial *vs*. marine settings (e.g., Chukhrov and Gorshkov, 1981; Dixon and Skinner, 1992; Manceau et al., 2007a,b). The necessity for a high ionic strength is also demonstrated in the work to date, where relatively low concentrations of $MgCl_2$ (~0.01 M) result in an intermediate birnessite with an interlayer spacing that is somewhat larger (e.g., Cui et al., 2006) than that typically observed in natural todorokite (e.g., Bodeï et al., 2007).

Classically, the transformation of birnessite to todorokite is described as a topotactic process, during which some of the morphological features and structural elements of the precursor phyllomanganate are preserved in the neo-formed todorokite (e.g., Bodeï et al., 2007; Feng et al., 2010). Structural incorporation of heterovalent cations, including Cu(II) and Ni(II), is thought to aid transformation (Burns and Burns, 1978a; Burns and Burns, 1979; Usui, 1979; Takematsu et al., 1984), as is the presence of structural Mn(III) where, because of its Jahn-Teller distortion, Mn^{3+}-O-Mn^{4+} bonds that run parallel to the eventual [010] direction in todorokite (space group p2/m) should be relatively weak and most susceptible to topotactic rearrangement (Bodeï et al., 2007; Cui et al., 2008; Zhao et al., 2015). However, the specific mechanistic details of the transformation were largely unclear. Recently, we report a new nucleation and growth model for the formation of todorokite in the marine environment (Atkins et al., 2014). The initial nucleation and growth stages likely occur simultaneously and are initiated by a thermally-induced kinking of the birnessite layers in nano-domains that act as nucleation sites for the formation of todorokite primary particles, where a significant proportion of structural Mn(III) and semi-coherent c-axis ordering are prerequisites for todorokite formation (Atkins et al., 2014). Todorokite primary particles then grow along the direction of tunnel growth ([010] crystallographic direction) via dissolution-recrystallization and assemble spontaneously via oriented attachment (OA), attaching at crystal faces perpendicular to the direction of tunnel growth ([100] crystallographic direction), to form large laths of todorokite (Atkins et al., 2014). The process likely

155 culminates in a traditional ripening of the neo-formed todorokite crystals, commencing
156 after the complete transformation of the birnessite precursor (Atkins et al., 2014).

157 While this new model explains many of the unique morphological and structural
158 features observed in natural todorokites, it also raises important questions about the long-
159 term sequestration of trace metals during phyllomanganate transformation and todorokite
160 crystal growth. In addition to todorokite, there is now a diverse and rapidly growing
161 catalogue of minerals known to grow via OA, including TiO_2, Cu and Fe (hydr)oxides,
162 ZnS, cryptomelane-type Mn oxide and $CaSO_4$ (Penn and Banfield, 1998a,b; Penn and
163 Banfield, 1999; Banfield et al., 2000; Gilbert et al., 2003; Huang et al., 2003; Waychunas
164 et al., 2005; Portehault et al., 2007; Burrows et al., 2012; Van Driessche et al., 2012;
165 Frandsen et al., 2014). Many of these minerals are ubiquitous in natural soils and
166 sediments and play important roles in the biogeochemical cycling of trace metals, yet to
167 date there have been few studies investigating the effects of OA type-growth on the
168 retention of sorbed trace metal impurities. In our recent work, we propose that, contrary to
169 traditional understanding, only structurally incorporated heterovalent cations with Jahn-
170 Teller distortion, resulting in the relatively weak metal-O-Mn^{4+} bonds necessary to
171 facilitate phyllomanganate layer kinking, will promote the nucleation of todorokite and
172 subsequent formation of todorokite primary particles (Atkins et al., 2014). We suggest that
173 for Ni-sorbed phyllomanganates (where Ni(II) is not Jahn-Teller distorted) Ni(II) will
174 slow the transformation of birnessite to todorokite, and be released to solution, in order
175 that transformation can proceed. Indeed, it has been noted that natural todorokite typically
176 contains significantly less Ni compared to the 10 Å phyllomanganate from which it
177 crystallized (Siegel and Turner, 1983; Bodeï et al., 2007).

178 Considering the few studies to investigate the fate of sorbed trace metals during
179 OA-type crystal growth, Kim et al. (2008) find that the progressive adsorption of Cu(II),
180 Zn(II), As(V) and Hg(II) onto nanoparticulate goethite surfaces disrupts growth via OA,
181 by essentially blocking attachment and aggregation interfaces. Similarly, Burrows et al.
182 (2012) find that the growth rate of goethite nanorods via OA is inhibited due to the
183 association of NO_3^- with the aggregating crystal faces. These authors conclude that if
184 nanoparticle growth by OA is to proceed, impurities at aggregation interfaces must either
185 be structurally incorporated into the mineral structure or desorbed into solution. For
186 poorly crystalline phyllomanganates however, because the octahedral layers are only a
187 single Mn octahedron thick, impurities incorporated into the crystal structure are
188 effectively still present at aggregation interfaces and so potentially still able to disrupt OA

189 (Atkins et al., 2014). These recent studies provide evidence to suggest that sorbed trace
190 metal impurities might slow transformation and/or be desorbed into solution in mineral
191 systems that grow via OA-type mechanisms.

192 In order to determine the effect of Ni on todorokite nucleation and growth, and
193 investigate the mobility and fate of Ni sequestered by birnessite during its transformation
194 into todorokite, we synthesize todorokite from a Ni-sorbed c-disordered hexagonal
195 birnessite, via a mild reflux procedure. Our Ni-sorbed birnessite precursor is analogous to
196 marine birnessite and displays sufficient ordering of the phyllomanganate layers along the
197 c-axis to enable the identification of key spectral, structural and morphological features in
198 the precursor c-disordered birnessite, 10 Å phyllomanganate intermediate and
199 transformation products. The birnessite, 10 Å phyllomanganate and subsequent
200 transformation products are extensively characterized including X-ray diffraction (XRD),
201 and high-resolution transmission electron microscopy (HR-TEM), while the mobility and
202 fate of Ni during the conversion is determined via HR-TEM energy dispersive
203 spectroscopy (HR-TEM EDS), Ni K-edge extended X-ray absorption fine structure
204 (EXAFS) spectroscopy and inductively coupled plasma optical emission spectrometry
205 (ICP-OES). In addition, we use μX-ray fluorescence (μXRF) and μEXAFS to determine
206 the dominant Mn oxide mineralogy and Ni mineralogical phase associations in a suite of
207 natural marine ferromanganese precipitates, namely a hydrogenetic crust, a diagenetic
208 nodule and a hydrothermal-type deposit. With careful and combined analysis of our work
209 we determine the effect of sorbed Ni on, and its mobility and fate during, the
210 transformation of birnessite to todorokite, and use our findings to shed light on the cycling
211 of Ni sequestered by birnessite in oxic marine sediments.
212
213
214 **2. EXPERIMENTAL METHODS**
215 **2.1 Preparation of Ni-Sorbed Hexagonal Birnessite Precursor**

216 Ni-sorbed c-disordered hexagonal birnessite with an interlayer spacing of ~7 Å and
217 ~1 wt% Ni was synthesized following a modified method of Villalobos et al. (2003).
218 Briefly, 320 mL of a 0.196 M $KMnO_4$ solution was added slowly to 360 mL of 0.51 M
219 NaOH solution. Subsequently ~3.4 g of $Ni(NO_3)_2$ was added to 320 mL of a 0.366 M
220 $MnCl_2$ solution and added slowly to the above mixture whilst stirring vigorously at room
221 temperature. After 30 min 5x 1 mL suspension aliquots were taken in order to quantify the
222 amount of mineral precipitated. The mineral suspension was then left to settle for ~4 hr,

223 after which the remaining supernatant was subsequently discarded and the wet mineral
224 slurry centrifuged at 3200 g for 30 min. After centrifugation, the wet slurry was washed:
225 initially 4 times by mixing with 1 M NaCl, with the first 3 washes shaken for 45 min and
226 the last wash adjusted to pH 8 and shaken overnight; then finally 10 times, 1x for 1 hr, 8x
227 for 0.5 hr and 1x overnight, by mixing with Milli-Q water (MQ); with all suspensions
228 centrifuged at 3200 g for 10 min. Approximately ¼ of the total resulting wet paste was
229 sacrificed for ICP-OES, to determine the total concentration of Ni sequestered to the solid
230 product, XRD, HR-TEM, BET surface area analysis and EXAFS spectroscopy. For ICP-
231 OES, aliquots of the sacrificed wet paste were dissolved in 3 M HCl and analysed for Ni
232 at the Trace Element Laboratory in the Department of Chemistry at the University of Hull,
233 using an Optima 5300 DV. Sample standard deviation is calculated based on measurement
234 of 3 separate aliquots. Our birnessite precursor contained ~1 wt% Ni (Table 1).
235
236 **2.2 Transformation of Ni-Sorbed Hexagonal Birnessite to Todorokite**
237 Our Ni-sorbed birnessite was transformed to todorokite following the method of
238 Atkins et al. (2014), originally adapted from Feng et al. (2004, 2010). Briefly, the wet
239 paste Ni-sorbed birnessite was suspended in ~4 L of 1 M $MgCl_2$ and stirred moderately for
240 18 hr at room temperature before centrifuging to a wet paste. This produced a Ni-sorbed
241 10 Å phyllomanganate which was re-suspended in ~800 mL of 1 M $MgCl_2$ in a 1 L round
242 bottom flask fitted with a glass condenser. The suspension was stirred continuously and
243 heated to and kept at 100 °C using a combined heating mantle with magnetic stirrer. The
244 suspension was then left to age under reflux for 4 wk, during which time suspension
245 aliquots (~75 mL) were extracted at 3, 6, 12, 24, 48 and 72 hr, 5 days, and 1, 2 and 4 wk.
246 Each aliquot was cooled in a water bath to room temperature before centrifuging at 3200 g
247 for 10 min. Supernatant solutions were collected and the pH measured (calibrated to
248 ±0.05 pH units with Whatman NBS grade buffers). Triplicate aliquots of each supernatant
249 solution were filtered through 0.2 µm syringe filters and retained for Ni and Mn analysis
250 via ICP-OES as above. All solid samples were washed extensively in 18.2 MΩ.cm MQ
251 water and oven dried at 30 ^{o}C, after which aliquots were subject to total digest for ICP-
252 OES as above, XRD, HR-TEM, BET surface area analysis and EXAFS spectroscopy as
253 below. It should be noted that Ni and Mn solution analysis, Ni total digest analysis and
254 BET surface area were not measured at the 2 wk reflux time point.
255
256

2.3 Natural Ferromanganese Samples

A hydrogenetic crust (237KD; Pacific Ocean; location: 09°18'N, 146°03'W; water depth: 4830 m), diagenetic nodule (Nod-P-1; Pacific Ocean; location: 14°50'N, 124°28'W; water depth: 4300 m) and hydrothermal deposit (D17-1-IV; Lau Basin; location: 22°17.78'S, 176°38.89'W; water depth: 2063-1965 m) sample were supplied by J.R. Hein (United States Geological Survey). **A** small section (~ 20 mm in length and perpendicular to the growth layers, 15 mm wide and 5 mm deep) from the upper 0-60 mm of each bulk sample was cut using a wafering saw, and a small amount of material was extracted using a micro drill, ground to a fine powder and dissolved in 6 M HCl, and analysed for bulk Ni content by ICP-OES as above. Bulk Ni contents for the hydrogenetic, diagenetic and hydrothermal samples are ~0.4, 0.5 and 0.07 wt.% Ni, respectively. The sections were subsequently encased in high purity resin and self-supported ~30 μm thick polished sections were prepared for μXRF and μEXAFS (Peacock and Moon, 2012). Previously reported chemical analyses of the hydrogenetic, diagenetic and hydrothermal samples give bulk Mn:Fe ratios of 1.9, 5 and 114, respectively, which are within the ranges expected for ferromanganese precipitates assigned to these different genetic types (Rehkämper et al., 2002).

2.4 Characterization of Precursor, Intermediate and Reflux Products

Powder XRD patterns were collected using a Bruker D8 diffractometer, operating at 40kV/40mA and equipped with CuKα radiation (λ = 1.5418) and a LynxEye detector. Samples were analyzed over 2-90 $^{o}2\theta$ with a 0.009^{o} step size and step count time of 7 sec. Data evaluation was undertaken using the DIFFRAC plus EVA software package. For the natural ferromanganese samples, distinctly Mn-rich regions of the samples (i.e., dark brown/black areas) were chosen to avoid obviously Fe-rich areas.

HR-TEM images were collected at the Leeds Electron Microscopy and Spectroscopy center in the Institute for Materials Research at the University of Leeds. Finely crushed powder samples were suspended in methanol and dispersed via sonication. Samples were then loaded onto individual holey carbon TEM grids and dried at room temperature. Imaging was performed at 200 kV on a Philips CM200 FEGTEM. EDS data was collected at several points of interest using the TEM. The wt% of Ni identified at each specific point of interest was measured using a standardless procedure where the errors associated with each wt% are given as the standard deviation of triplicate measurements, but the absolute limit of detection cannot be quantified. It is important to note that while

291 our EDS data can be used for relative comparison of Ni concentrations between measured
292 points, it cannot be used as a quantitative measure of absolute Ni concentrations.
293 Specific surface area of all samples was measured using the BET-N_2 method using
294 a Gemini V2365 system (Micromeritics Instrument Corp.). Samples were dried and
295 degassed at room temperature for 24 hr. Reported BET values are ±5 %.
296
297 **2.5 X-ray Absorption and Fluorescence Spectroscopy**
298 We collected Ni K-edge (8.333 keV) EXAFS spectra for our Ni-sorbed birnessite,
299 10 Å phyllomanganate and subsequent reflux products. Micro-focus μXRF elemental
300 maps (for Mn, Fe and Ni) and μEXAFS (at the Ni and Mn-K edges (6.539 keV)) were also
301 collected for the natural ferromanganese samples. Spectra were collected at Diamond
302 Light Source (DLS) Ltd. on station B18 (synthetic samples) and I18 (natural samples).
303 During data collection, storage ring energy was 3.0 GeV and the beam current was
304 approximately 200 mA. Samples were presented to the X-ray beam as dry powders
305 pressed into pellets (synthetic samples), or as ~30 μm thick self-supported thin sections
306 (natural samples), held between Kapton tape. Data was acquired in fluorescence mode (Ni
307 K-edge) or transmission mode (Mn K-edge). We saw no photo-redox or visible beam
308 damage on the samples after 6 EXAFS scans to k = 14 $Å^{-1}$ but in order to minimize beam
309 damage we recorded 4 spectra at a single x,y point before moving to a new point to record
310 a further 4 spectra, collecting a total of 36 spectra (for Ni K-edge of the synthetic samples)
311 or up to 9 spectra (9 for Ni K-edge and 4 for Mn K-edge of the natural samples). μXRF
312 maps were collected at 8.4 keV with a pixel size of 10x10 μm and a count time of 1 sec
313 per pixel. Maps were deadtime corrected and registered using custom beamline software.
314 Maps were used to identify points of interest (POI) with positive Ni-Mn correlations, for
315 collection of Ni and Mn μEXAFS. For μEXAFS the beam spot was ~2x3 μm. Energy
316 calibration was achieved by assigning the first inflection point of Au (L3) foil to 11.919
317 keV.
318 EXAFS data reduction was performed using ATHENA (Ravel and Newville,
319 2005) and the Ni spectra were fit using DL_EXCURV (Tomic et al., 2005). Spectra were
320 fit in k-space over 3 – 12 $Å^{-1}$, with no Fourier filtering, and the fitting included full
321 multiple scattering as coded in EXCURV98 (Binsted, 1998). Multiple scattering
322 calculations require specification of the full three dimensional structure of the Ni
323 coordination environment (i.e., bond lengths and angles). This was done using
324 hypothetical model clusters with either C_1 or C_3 symmetry, for various different Ni local

coordination geometries, including Ni adsorbed at Mn octahedral vacancies in the phyllomanganate layers (Peacock and Sherman, 2007b), Ni structurally incorporated into the phyllomanganate layers (Peacock and Sherman, 2007a,b) and Ni sorbed to todorokite (Fig. 1). Several reference compounds were used to help fit the EXAFS spectra, namely a synthetic Ni-sorbed c-disordered birnessite where Ni is surface adsorbed at the vacancies, a natural Ni-incorporated poorly crystalline phyllomanganate where Ni is structurally incorporated, and two Ni-sorbed todorokite samples prepared at 24 hr and 1 wk contact times (section 2.6). The reference spectra were fit by refinement of a single model cluster. Where appropriate, the sample spectra were fit by linear combination of different model clusters as coded in EXCURV98 (Binsted, 1998). Linear combination was performed over the k-range 3 – 12 $Å^{-1}$ with a linear combination of the k^3-weighted Chi(k) for each cluster. In the linear combinations only EF and relative site occupancies were optimized. For all fits, the number of independent data points (N_{ind}) was determined using Stern's rule (Stern, 1993) as $2\Delta k\Delta R/\pi + 1$ (Booth and Hu, 2009) where Δk and ΔR are the range in k and R-space actually fitted. The number of fitted parameters (N_{par}) was determined as the total number of parameters optimized during the various model refinements and was always less than N_{ind}.

We also performed linear combination fitting for some of the Mn spectra recorded for the natural ferromanganese samples in ATHENA. In these cases fitting was done with a linear combination of the Chi(k) for the δMnO_2 and todorokite reference spectra, over the k-range 3 – 12 $Å^{-1}$, and without constraining the component sum to equal 1.

For the Ni spectra, fit in DL_EXCURV, the quality of the fits provided by the different model clusters was assessed using the EXAFS R-factor and the reduced Chi^2 function, which provides an absolute index of goodness of fit (and so can be used for comparing fit quality between fits where N_{par} is not equivalent; all as coded in EXCURV98 (Binsted, 1996, 1998)). For the Mn spectra, fit in ATHENA, the errors reported are those typically applied to 2-component mixtures (e.g., Kim et al., 2000). The errors associated with the EXAFS modelling and linear combination fits are described in detail in the Supplementary Information (section S2.5).

2.6 Reference Compounds

A range of Ni-free synthetic Mn oxides were prepared as described in Atkins et al. (2014) and used as references during the above analyses, including triclinic Na-birnessite (Tc-Na-birnessite), crystalline hexagonal birnessite (Hx-birnessite), c-disordered

359 hexagonal birnessite, all with an interlayer spacing of ~7 Å, δMnO_2 and crystalline
360 todorokite. Mineral identity and purity was confirmed by XRD analysis of randomly
361 orientated powder samples.
362 The Ni-sorbed Mn oxides used as references during the EXAFS analysis included
363 a Ni-sorbed c-disordered birnessite, a Ni-incorporated natural poorly crystalline
364 phyllomanganate, and Ni-sorbed todorokite. Preparation of the Ni-sorbed birnessite and
365 todorokite reference samples is described in the Supplementary Information (section
366 S2.6). The natural phyllomanganate is catalogued as hydrogenetic ferromanganese crust
367 sample 5DSR8 (Pacific Ocean; location: 04°09'S, 174°54'W; water depth: 1585 m) from
368 Chu (2004), and was sourced from the National Oceanography Centre, Southampton as a
369 dry powder with no further preparation performed.
370
371
372 **3. RESULTS**
373 **3.1 Transformation of Ni Sorbed Hexagonal Birnessite to Todorokite**
374 *3.1.1 X-ray diffraction*
375 XRD patterns for our Ni-sorbed birnessite, 10 Å phyllomanganate and all
376 subsequent reflux products are shown in Figure 2. The diagnostic XRD features for our
377 birnessite, 10 Å phyllomanganate and todorokite are discussed in Atkins et al. (2014) and
378 summarised here in the Supplementary Information (section S3.1.1).
379 Our birnessite shows 4 broad peaks at ~7.2 Å, ~3.6 Å, ~2.4 Å and ~1.4 Å,
380 corresponding to the [001], [002], [100] and [110] basal reflections, respectively (for
381 reference pattern see turbostratic birnessite, Drits et al., 1997). Following suspension in 1
382 M $MgCl_2$, the interlayer spacing is expanded from ~7 Å to ~10 Å as indicated by the
383 appearance of peaks at ~9.6 Å, ~4.8 Å and ~3.2 Å ([001] [002] and [003] basal
384 reflections, respectively) in our 10 Å phyllomanganate (for reference pattern see buserite
385 JCPDS-32-1128). For both phases, the slight degree of asymmetry on the high angle side
386 of the ~2.4 Å peak indicates a lack of periodic ordering (Villalobos et al., 2006), however,
387 in agreement with our previous work, the basal reflections of our 10 Å phyllomanganate
388 are more intense than those of the birnessite suggesting that the ion-exchange process
389 enhances the crystallinity and long range ordering of the layers (Atkins et al., 2014). For
390 both our birnessite and 10 Å phyllomanganate, the $d100/d110$ peak intensity ratios are
391 close to $\sqrt{3}$ (at 2.42/1.41 and 2.40/1.41, respectively), and the 1.4 Å peak is symmetrical,

indicating that both phases have hexagonal layer symmetry with $a = b = 2.83$ Å (Drits et al., 1997).

Over the course of the reflux there is little evidence for the formation of todorokite (JCPDS-38-475) during the first 24 hr (Fig. 2). The four distinct changes in the XRD patterns, expected during the transformation of birnessite to todorokite (Atkins et al., 2014; section S3.1.1), only start to become visible by 48 hr reflux (Fig. 2). Firstly, by 48 hr reflux we observe broad characteristic todorokite peaks at ~2.2 Å, ~1.9 Å and ~1.7 Å, and a broad hump at ~1.5 Å, indicating that transformation of the 10 Å phyllomanganate to todorokite has begun (Feng et al., 2004; Atkins et al., 2014). As the reflux proceeds these peaks become sharper and more intense indicating the progressive formation of todorokite. Secondly, by 48 hr reflux the peak at ~2.4 Å has begun to split to reveal a shoulder at ~2.45 Å, which becomes more prominent with time. Thirdly, the peak at ~5 Å has begun to broaden, developing into a broad shoulder on the high-angle side at ~4.3 Å. Fourthly, the peak at ~1.4 Å has started to become progressively asymmetrical. These later three changes are those expected during the transformation of 10 Å phyllomanganate into todorokite (Feng et al., 2010; Atkins et al., 2014).

3.1.2 Transmission electron microscopy

HR-TEM images are shown in Figure 3 and highlight the gradual transformation of our 10 Å phyllomanganate into todorokite over the first 2 wk of reflux. Our 10 Å phyllomanganate has a rumpled plate-like morphology, where the edges of the layers measure ~5-7 nm wide (Fig. 3a, inset). Repetition of the [001] lattice planes indicates that the individual layers are reasonably well stacked over at least 3 nm. The measured interlayer of the 10 Å phyllomanganate is equal to ~0.82 nm (Fig. 3b), which although inconsistent with that measured via XRD (0.96 nm; Fig. 2), is consistent with the partial collapse of the layers under the high vacuum conditions of the TEM (e.g., Post and Veblen, 1990; Atkins et al., 2014). At 6 hr reflux the morphology is still dominated by the platy 10 Å phyllomanganate phase (Fig. 3c,d), however, small primary particles of todorokite elongated longitudinally along the direction of tunnel growth ([010]) and measuring ~6-10 nm wide across the direction of tunnel growth ([100]) are also visible within the sample matrix (Fig. 3c,d). These particles display poorly defined lattice fringes (Fig. 3c.d), and are therefore only poorly crystalline, consistent with the lack of todorokite XRD peaks in the first few hours of reflux (Fig. 2). At 24 hr reflux, the mineralogy is still dominated by the 10 Å phyllomanganate, however, the todorokite primary particles have

begun to form platy todorokite aggregates measuring ~200x200 nm (Fig. 3e), and in particular, large laths of todorokite measuring ~250 nm in length (along the direction of tunnel growth) and ~70 nm wide (across the direction of tunnel growth) (Fig. 3f). These laths are assembled from a number of smaller primary particle building blocks that vary in length but measure consistently between ~8-10 nm wide. With increasing reflux time, these secondary laths increase in size, particularly in the longitudinal direction, and after 1 wk we see large laths which dominate the overall morphology, measuring on average ~460 nm long and ~70 nm wide (Fig. 3g). By 1 wk reflux, we also see that individual laths are aligned with each other at 120° to form large aggregates of todorokite that exhibit a plate-like morphology (Fig. 3h). These large plates (>1000x500 nm), orientated in three distinct directions, are arranged into stacked layers along the [001] direction (Fig. 3h). By 2 wk reflux, the average size of the laths has increased further to ~700 nm long and ~150 nm wide, and the lattice fringes of the laths are notably more defined, indicating an increase in the crystallinity of the neo-formed todorokite with time (Fig. 3i,j); we are also unable to find any 10 Å phyllomanganate or phyllomanganate-like phase within the sample matrix, indicating that by this time point the 10 Å phyllomanganate has undergone essentially complete transformation into todorokite (multiple sub-samples of the solid extracted at this time point were scanned over extended areas, with images typified by Fig. 3i,j).

EDS data collected at 6 and 24 hr, and 1 and 2 wk reflux, for selected points (marked on Fig. 3, where point 1 and 2 are on the 10 Å phyllomanganate and todorokite matrix, respectively), is shown in Table 2 and provides a relative measure of Ni concentration and distribution in the 10 Å phyllomanganate and todorokite phases (section 2.4). From 6 hr to 1 wk reflux, despite the progressive formation of todorokite, the majority of the sequestered Ni in the measured sample points is associated with the 10 Å phyllomanganate and there is no detectable Ni associated with the todorokite primary particles or laths (Table 2). At 2 wk reflux, when there is no observable 10 Å phyllomanganate or phyllomanganate-like phase within the sample matrix, there is similarly no detectable Ni associated with todorokite (where several points on a number of different todorokite laths and plate-like aggregates were measured, all typified by the 2 wk EDS point, Fig. 3i, Table 2). Overall our EDS data can be interpreted to indicate that, of the solid-associated Ni, there is relatively more Ni associated with the transforming phyllomanganate compared to the neo-forming todorokite. EDS spectra are shown in Figure S1 (Supplementary Information).

460

461 *3.1.3 Physiochemical characterisation*

462 The absolute measurements of Ni wt% in our birnessite, 10 Å phyllomanganate
463 and subsequent reflux products are shown in Table 1. Surface area, reaction solution Mn
464 and Ni concentration, and pH are shown in Table 3 and/or Figure 4. The absolute
465 concentration of Ni associated with the solid phase shows little variation from the
466 birnessite to the 10 Å phyllomanganate, and subsequently up to and including the first 72
467 hr of reflux, with our birnessite containing 0.92±0.002 wt% Ni and our 72 hr sample
468 containing 0.98±0.010 wt% Ni (Table 1). The concentration of Ni associated with the
469 solid phase drops to 0.80±0.011 wt% Ni by 1 wk and the final todorokite product contains
470 0.54±0.003 wt% Ni by 4 wk reflux. Overall we observe a ~50 % reduction in the
471 concentration of Ni sequestered to the solid product over the duration of the reflux.

472 Dissolved [Mn] in the reaction solution shows an initial spike from 0.003 mM by 3
473 hr, to 0.017 mM by 6 hr, remaining relatively constant up to and including 24 hr, and
474 subsequently decreasing to 0.01 mM by 48 hr reflux (Fig. 4, Table 3). This initial spike is
475 followed by a relatively gradual overall decrease towards the final time point, with [Mn] at
476 4 wk comparable to that measured at 3 hr reflux. Consistent with the decrease in solid-
477 associated Ni during the course of the 4 wk reflux, dissolved [Ni] in the reaction solution
478 increases from 0.004 mM by 3 hr to 0.093 mM by 4 wk reflux.

479 The surface area of the 10 Å phyllomanganate is 102.3 m^2/g, which decreases to
480 84 m^2/g by 3 hr, with little variation during the first 12 hr, then increases to 97 and 99
481 m^2/g by 24 and 48 hr, respectively, with a second and more substantial drop to 37 m^2/g by
482 1 wk reflux. Surface area then continues to decrease to 20 m^2/g by the full 4 wk reflux.
483 Overall we observe an ~80 % reduction in surface area over the duration of the 4 wk
484 reflux (Fig. 4).

485 The pH of the cooled reaction solutions shows a slight increase from pH ~5.29 to
486 5.93 over the first 72 hr of reflux, then remains relatively stable until a more substantial
487 drop occurs from pH ~5.81 at 1 wk to ~4.26 at 4 wk reflux (Table 3).

488

489 *3.1.4 Ni K-edge X-ray absorption spectroscopy*

490 *3.1.4.1 Reference compounds*

491 Ni K-edge EXAFS and Fourier transforms for the reference compounds are shown
492 in Figure 5 and fits are summarized in Table 4. Visual inspection of the Ni-sorbed
493 birnessite and Ni-incorporated natural phyllomanganate reference spectra indicate that the

494 Ni local coordination environment is very similar to that found previously for Ni adsorbed
495 to hexagonal birnessite, where Ni is located at Mn octahedral vacancy sites present in the
496 phyllomanganate layers (Peacock and Sherman, 2007a,b; Peacock, 2009; Peña et al.,
497 2010), and Ni-rich marine ferromanganese precipitates were Ni is found entirely
498 structurally incorporated into the phyllomanganate layers (Peacock and Sherman, 2007a,b;
499 Peacock, 2009), respectively. In agreement with this previous work, the best fits to our
500 Ni-sorbed and Ni-incorporated reference spectra are provided by optimization of the
501 model clusters representing Ni adsorbed at vacancies and Ni incorporated into the
502 phyllomanganate layers, respectively (Fig. 5, Table 4).

503 In contrast to Ni adsorbed on and incorporated into birnessite, there has been very
504 little work to determine the crystal-chemical mechanism of Ni uptake by todorokite.
505 Theoretically, trace metals could sorb to todorokite via outer-sphere surface complexation,
506 where Ni might be located in the todorokite tunnels (e.g., Pakarinen et al., 2010), or via
507 inner-sphere surface complexation, where Ni could adsorb to Mn(OH) sites present at the
508 edges of the triple chains that form the todorokite framework, akin to Ni adsorption on
509 triclinic birnessite in which there are no Mn octahedral vacancy sites (Peacock and
510 Sherman, 2007b), and at high Ni loading on hexagonal birnessite when the vacancy sites
511 are saturated (Manceau et al., 2007a). Sorbed as an outer-sphere complex, the Ni-sorbed
512 todorokite EXAFS spectrum would resemble that of Ni^{2+}(aq) where Ni is surrounded by 6
513 O at ~2.04±0.02 Å (e.g., Xu et al., 2007). Adsorbed at the Mn(OH) sites, the Ni-sorbed
514 todorokite spectrum would likely reflect Ni adsorbed as either a tridentate corner-sharing
515 complex, as per Ni adsorbed on triclinic birnessite with 2 Mn at ~3.05±0.05 Å (Peacock
516 and Sherman, 2007b), a bidentate corner-sharing complex with 2 Mn at ~3.49±0.11 Å, as
517 per Ni adsorbed on hexagonal birnessite (Manceau et al., 2007a), or possibly a bidentate
518 edge-sharing complex with 1 Mn at ~3.00±0.10 Å, as is reported for Cu(II) adsorbed on
519 ferrihydrite (Scheinost et al., 2001; Moon and Peacock, 2012). To our knowledge, there
520 are no EXAFS data for Ni structurally incorporated into todorokite, but Ni is expected to
521 exclusively occupy the Mn sites at the edges of the triple chains (Post and Bish, 1988;
522 Post et al., 2003; Bodeï et al., 2007), which would yield an Ni coordination environment
523 consisting of 6 O at ~2.04 Å, 4 edge-sharing Mn at ~2.87-2.91 Å and 4 corner-sharing Mn
524 at ~3.48-3.50 Å (Bodeï et al., 2007). Visual inspection of our todorokite sorption spectra
525 at 24 hr and 1 wk contact time show the Ni local coordination environment is very similar
526 in both spectra and most similar to Ni adsorbed on triclinic birnessite (Peacock and
527 Sherman, 2007b). Accordingly our best fits to these spectra are provided by the cluster

representing Ni tridentate corner-sharing to Mn(OH) sites present at the edges of the todorokite triple chains, and we find 6 O at ~2.00-2.11 Å and 2 Mn at ~2.98-3.10 Å. It should be noted that the fits were improved (from reduced Chi^2 ~18 to ~15, Table 4) by allowing a slight distortion of the Ni octahedron, evident as a very minor deviation of the spherical coordinates of the surface binding O atoms from exact octahedral coordination (O_1, O_4 and O_6, Table 4). The fits could not be improved by including any other Ni coordination environments.

3.1.4.2. Experimental samples

Ni K-edge EXAFS and Fourier transforms for the experimental samples are shown in Figure 6 and fits are summarized in Table 5. Spectra for our birnessite and 10 Å phyllomanganate are visually very similar to those in previous work where Ni is sorbed in two distinct coordination environments, namely, adsorbed as a surface complex at vacancies and also structurally incorporated into the phyllomanganate layers (Peacock and Sherman, 2007b; Peacock, 2009). When Ni is present as a structurally incorporated species in addition to a vacancy site adsorbed complex, the spectral shape of the characteristic *k*-space features for Ni adsorbed at vacancies, at ~6 and 8 $Å^{-1}$ (see the Ni-sorbed birnessite reference spectrum (Fig. 5)), are modified towards the shape of these features for Ni incorporated into the phyllomanganate layers (see the Ni-incorporated natural phyllomanganate reference spectrum (Fig. 5)). Specifically, the feature at ~6 $Å^{-1}$ deepens to produce a clear splitting of the ~5.5-7 $Å^{-1}$ oscillation, while the feature at ~8 $Å^{-1}$ shoals resulting in a single peak for the ~7.5-9 $Å^{-1}$ oscillation, both as a function of the amount of structurally incorporated Ni (Peacock, 2009). The presence of Ni as both surface adsorbed and structurally incorporated species is manifest in the Fourier transform as two next-nearest Mn neighbour distances represented by peaks at ~3.5 and 2.9 Å, respectively, whose relative amplitudes reflect the proportion of the total Ni occupying vacancy sites vs. structurally incorporated positions (Peacock, 2009). Accordingly the best fits to the birnessite and 10 Å phyllomanganate spectra are provided by a linear combination of the Ni-sorbed birnessite and Ni-incorporated natural phyllomanganate reference spectra (Fig. 6, Table 5). Specifically, we find that our birnessite contains ~54±4 % Ni adsorbed at vacancy sites and ~46±4 % Ni structurally incorporated, while our 10 Å phyllomanganate contains ~38±4 % Ni at vacancies and ~62±4 % Ni incorporated. The increase in the proportion of structurally incorporated Ni from our birnessite to 10 Å phyllomanganate is consistent with the observed increase in long range

order between our precursor and intermediate phases (Fig. 2). Partial dissolution-recrystallization during Mg ion exchange is expected to favour structural incorporation of surface adsorbed species (e.g., Bodeï et al., 2007).

The reflux spectra are visually very similar to our birnessite and 10 Å phyllomanganate, and remarkably similar to each other, up to and including 1 wk reflux (Fig. 6). These observations indicate that the Ni local coordination environment in the reflux samples is likely similar to that in the precursor and intermediate samples, and that this environment does not significantly change throughout the reflux to 1 wk. In particular, these reflux spectra do not resemble our reference spectra for Ni-sorbed todorokite (Fig. 5). Neither is there any indication that a significant proportion of the Ni has become structurally incorporated into the neo-forming todorokite. In this latter scenario, one would expect a change in the amplitude of the characteristic spectral features resulting from edge- and corner-sharing Mn. Specifically, if a significant proportion of the Ni originally associated with our 10 Å phyllomanganate was incorporated into the neo-forming todorokite then the amplitude of the spectral features at ~6 and 8 $Å^{-1}$ in *k*-space, which manifest as Ni-Mn distances at ~2.9 and 3.5 Å in *R*-space, should change somewhat to reflect the fact that the local coordination environment of the Ni now includes 6 Mn at ~2.9 Å and 2 Mn at ~3.5 Å, as expected for Ni coprecipitated with a phyllomanganate, and also 4 Mn at ~2.9 Å and 4 Mn at ~3.5 Å, as expected for Ni incorporated into todorokite (Bodeï et al., 2007). While this change in the Ni local coordination environment would not produce significant changes in the expected Ni-Mn interatomic distances, and the absolute changes in the number of Mn next-nearest neighbours would be difficult to resolve, the fact that the amplitude of these key spectral features, and in fact the entire spectral signature, remains so remarkably consistent from 3 hr to 1 wk reflux is strong indication that Ni remains sequestered by our 10 Å phyllomanganate as the reflux proceeds, in agreement with our HR-TEM EDS (Table 2), and despite the fact that our XRD (Fig. 2) and HR-TEM (Fig. 3) show a significant amount of neo-formed todorokite present in the sample matrix by 48 hr reflux. In agreement with these observations, the best fits to the spectra for 3 hr to 1 wk reflux are provided by a linear combination of the Ni-sorbed birnessite and Ni-incorporated natural phyllomanganate reference spectra, as per our birnessite and 10 Å phyllomanganate samples (Fig. 6, Table 5). Specifically, we find that of the total Ni sorbed, ~40 % is adsorbed at the vacancy sites with ~60 % structurally incorporated, with no significant change in these proportions when comparing the reflux samples to the 10 Å phyllomanganate sample, or each other.

Consistent with the absence of 10 Å phyllomanganate or a phyllomanganate-like phase in our HR-TEM images by 2 wk reflux, the 2 wk and 4 wk reflux spectra are visually very different to our birnessite, 10 Å phyllomanganate and the reflux spectra up to and including 1 wk (Fig. 6). Instead the 2 wk and 4 wk spectra are visually very similar to our reference spectra for Ni-sorbed todorokite where Ni is sorbed via tridentate corner-sharing surface complexes with 6 O at ~2.00-2.11 Å and 2 Mn at ~2.98-3.10 Å. (section 3.1.4.1; Table 4; Fig. 5). There is no obvious visual evidence for Ni-Mn edge- or corner-sharing distances at ~2.9 Å or ~3.5 Å indicative of Ni structurally incorporated into a phyllomanganate (~2.9 Å), adsorbed at vacancy sites on a phyllomanganate (~3.5 Å), or structurally incorporated into todorokite (~2.9 and 3.5 Å). Accordingly our best fits to these spectra are provided by refining the reference spectra for Ni-sorbed todorokite, resulting in refined parameters of 6 O at ~1.98-2.10 Å and 2 Mn at ~2.94-3.11 Å. The fits could not be improved by including any other Ni coordination environments. Because the Mn(OH) sites present at the edges of the todorokite triple chains and those at the edges of a phyllomanganate layer essentially provide the same local coordination environment for sorbed trace metals, the presence of Ni in tridentate corner-sharing configuration could indicate that Ni is newly associated with the neo-formed todorokite or in fact still associated with the 10 Å phyllomanganate, albeit via a different sorption mechanism compared to the previous reflux samples. However, the fact that we cannot identify any 10 Å phyllomanganate in our 2 wk samples (Fig. 3i,j) indicates that the solid-associated Ni at 2 wk and 4 wk reflux is most likely adsorbed to neo-formed todorokite.

3.2 Natural Ferromanganese Samples

3.2.1 Bulk X-ray diffraction

Bulk XRD patterns for our hydrogenetic, diagenetic and hydrothermal ferromanganese precipitates are shown in Figure 7. The Mn mineralogy of our hydrogenetic crust and diagenetic nodule is dominated by very poorly crystalline phyllomanganate, usually termed vernadite in natural samples (JCPDS-15-604) and δ-MnO_2 in synthetic analogues, with also a contribution from very poorly crystalline 10 Å phyllomanganate (buserite JCPDS-32-1128). The $d100/d110$ peak intensity ratios approximately equal $\sqrt{3}$ indicating that the phyllomanganate layers have hexagonal symmetry with $a = b = 2.83$ Å (Drits et al., 1997). The presence of very poorly crystalline phyllomanganate phases in our hydrogenetic and diagenetic samples agrees with previous reports for these ferromanganese precipitate genetic types (e.g., Peacock and Sherman,

2007b). In particular, the presence of poorly crystalline 10 Å phyllomanganate in diagenetic ferromanganese precipitates is often reported in natural samples, where it is thought to have formed during mild dissolution-recrystallisation of poorly crystalline 7 Å phyllomanganate (e.g., Bodeï et al., 2007). Our hydrothermal sample consists of mixed 7 and 10 Å phyllomanganate and todorokite phases, with characteristic todorokite peaks at ~2.2 Å [21-2] and ~1.7 Å [21-4], and a splitting of the ~2.4 Å peak region as expected when 10 Å phyllomanganate and todorokite are mixed (Atkins et al., 2014; section S3.1.1). The relatively high intensity of the basal reflections for 7 Å phyllomanganate (and to some extent for 10 Å phyllomanganate, noting that these peaks also result from todorokite) indicates that the phyllomanganate layers are significantly more ordered than in our hydrogenetic and diagenetic samples. The presence of todorokite in hydrothermal ferromanganese precipitates is often reported in natural samples, where it is thought to have formed during diagenesis and mild hydrothermal alteration of 10 Å phyllomanganate (e.g., Peacock and Moon, 2012). Further details on the XRD of our natural samples are presented in the Supplementary Information (section S3.2.1).

3.2.2 µXRF elemental mapping

Two-colour and tri-colour µXRF maps of the distribution of Fe (green), Mn (blue) and Ni (red) in our natural ferromanganese samples are shown in Figure 8, with scatter plots of the normalized fluorescence counts between Fe-Mn, Mn-Ni and Fe-Ni in Figure 9. The relatively pure green and blue colours of the Fe- and Mn-rich areas of the Fe-Mn maps indicate that Fe and Mn are strongly spatially segregated and anti-correlated in the scanned areas of all 3 samples (Fig. 8a,c,e; with Pearson correlations for the Fe-Mn plots at r = -1.5, -0.34 and 0.13 for the hydrogenetic, diagenetic and hydrothermal samples, respectively (Fig. 9a,d,g)). This Fe-Mn spatial distribution is observed at every probed spatial scale in natural ferromanganese precipitates (e.g., Manceau et al., 2004). On adding Ni (red) to both the hydrogenetic and diagenetic samples, the Mn-rich areas turn varying shades of magenta (blue + red), while the Fe-rich areas remain bright green (green + red = yellow) (Fig. 8b,d), indicating that the majority of the Ni is spatially associated and positively correlated with the Mn-rich fraction in the scanned areas (with r Mn-Ni and Fe-Ni at 0.94 and -0.69 for the hydrogenetic sample (Fig. 9b,c) and 0.83 and -0.36 for the diagenetic sample (Fig. 9e,f), respectively). In contrast, on adding Ni (red) to the hydrothermal sample, there is little change in the colours of the Mn- or Fe-rich areas (Fig. 8f). Instead, small, intense red areas appear in the center left region of the map that show

664 little spatial correlation with either the Mn- or Fe-rich fractions (with *r* Mn-Ni and Fe-Ni
665 at -0.28 and 0.17, respectively (Fig. 9h,i)), indicating that the majority of the Ni is
666 predominantly concentrated in an unidentified mineral phase. The μXRF maps were used
667 to select 4 physically discrete and chemically defined POI enriched in Mn and Ni (Fig. 8)
668 that were subject to μEXAFS.
669
670 *3.2.3 μEXAFS*
671 Mn K-edge EXAFS of the Mn oxide reference compounds and μEXAFS of the
672 natural ferromanganese samples are shown in Figure 10. In agreement with previous
673 studies, our Mn oxide reference spectra show clear differences in *k*-space in the (6.5 – 9.5
674 $Å^{-1}$) indicator region (e.g., Webb et al., 2005a). For layered structures, the *k*-space peaks at
675 ~6.7, 8 and 9.2 $Å^{-1}$ appear sharper and more intense with an increase in coherent stacking
676 of the layers along the c-axis, i.e., from our δMnO_2 to Hx-birnessite (e.g., Webb et al.,
677 2005a). For tunnel structures, these indicator features are less sharp and intense and
678 significantly broader, with a notable increase in the background of the region between
679 ~7.4-8.7 $Å^{-1}$, and the shoulder at ~5.5 $Å^{-1}$ also appears less pronounced, compared to
680 layered structures (e.g., Webb et al., 2005a). These differences are evident when
681 comparing our phyllomanganates (δMnO_2, Hx-birnessite and Tc-Na-birnessite) to our
682 tectomanganate (high crystalline todorokite) reference spectra. In agreement with our
683 XRD (Fig. 7), the spectra for the hydrogenetic and diagenetic samples are most similar to
684 the reference spectrum for poorly crystalline phyllomanganate δMnO_2, while the spectral
685 features at ~6.7, 8 and 9.2 $Å^{-1}$ for the hydrothermal sample recorded at two separate POI
686 are less sharp and intense, and also broader, indicating the presence of todorokite. The
687 hydrothermal sample also shows an elevated background between ~7.4-8.7 $Å^{-1}$ and a
688 somewhat less pronounced shoulder at ~5.5 $Å^{-1}$, compared to the hydrogenetic and
689 diagenetic samples. Given our bulk XRD shows that the phyllomanganate present in the
690 hydrothermal sample is in fact more ordered than that found in our hydrogenetic and
691 diagenetic samples, then the reduced intensity and sharpness, along with the broadening,
692 of these indicator peaks is most likely due to the presence of todorokite rather than a very
693 poorly crystalline phyllomanganate phase. Linear combination of the δMnO_2 and
694 todorokite reference spectra indicate that the hydrothermal sample at POI1 and 2 contains
695 ~70±10 % δMnO_2 and ~30±10 % todorokite.
696 Ni K-edge μEXAFS of the natural ferromanganese samples are shown in Figure 11
697 and the fits are summarised in Table 6. For our hydrothermal sample at POI2 the Ni

concentration was too low to generate a useable EXAFS spectrum. Spectra for our hydrogenetic and diagenetic samples, containing predominantly poorly crystalline phyllomanganate, and our hydrothermal sample, containing both phyllomanganate and todorokite, are visually most similar to our reference spectrum for Ni structurally incorporated into a natural phyllomanganate (Fig. 5). In particular, we observe a pronounced splitting of the spectral feature at ~6 $Å^{-1}$ and a single peak at ~8 $Å^{-1}$ as expected for Ni incorporated into the phyllomanganate layers (Manceau et al., 2007b; Peacock and Sherman, 2007a,b; Peacock, 2009). In all spectra, the splitting of the feature at ~6 $Å^{-1}$, and the amplitude of the corresponding peak in the Fourier transform at ~2.9 Å, is not as pronounced or as intense, respectively, as that observed in the Ni-incorporated natural phyllomanganate reference spectrum. In this sense the natural ferromanganese *k*-space spectra also resemble the experimental samples up to and including 1 wk reflux (Fig. 6), where we find Ni both structurally incorporated in, and surface adsorbed to, a phyllomanganate (section 3.1.4.2). However, in our natural ferromanganese spectra, we do not observe a significant peak in the Fourier transform at ~3.5 Å corresponding to Ni surface adsorbed at the vacancy sites. As for the Ni-incorporated natural phyllomanganate reference spectrum, the very minor peak at ~3.5 Å is fit by multiple scattering occurring in the near-coordination environment about the Ni atom (Peacock and Sherman, 2007a; Peacock, 2009). Accordingly, the best fits to the natural ferromanganese samples are provided by the cluster representing Ni incorporated into the layers of a phyllomanganate (Fig. 11, Table 6). Inclusion of Ni in any other local coordination environments did not improve the fits. Complete structural incorporation of Ni into the layers of natural marine phyllomanganates agrees with previous work for other Ni-rich hydrogenetic and diagenetic ferromanganese precipitates (Peacock and Sherman, 2007a). Importantly, in our hydrothermal sample containing both phyllomanganate and todorokite, despite the fact our μXRF indicates that the majority of the sequestered Ni is associated with an unidentified phase, we are still able to detect the spectral signature for a minority of Ni structurally incorporated into a phyllomanganate at POI1, and there is no evidence to indicate that Ni is adsorbed or incorporated by the co-located todorokite. This suggests that, in agreement with our experimental results up to an including 1 wk reflux, in sediments where both phyllomanganate and todorokite are present, the majority of the Mn-bearing solid-phase Ni is preferentially sequestered by the phyllomanganate phase.

732 **4. DISCUSSION**

733 **4.1 Effect of Sorbed Ni on the Transformation of Birnessite to Todorokite**

734 We transform a Ni-sorbed 10 Å phyllomanganate where, of the total Ni sorbed (~1
735 wt% Ni), ~60 % is structurally incorporated into the phyllomanganate lattice with the
736 remaining ~40 % surface adsorbed at Mn octahedral vacancy sites present in the
737 phyllomanganate layers (Table 5a). However, despite the presence of both structurally
738 incorporated and surface adsorbed Ni, we find no evidence to suggest that this metal
739 impurity has a significant effect on the overall growth mechanism of todorokite,
740 previously established for our Ni-free system (Atkins et al., 2014). In contrast, we
741 observe a significant reduction in the overall growth rate of todorokite, compared to our
742 Ni-free system (Atkins et al., 2014). These effects are discussed below.

743

744 *4.1.1 Growth mechanism*

745 Our HR-TEM images clearly show the presence of todorokite primary particles
746 (by 6 hr reflux; Fig. 3c,d) that are elongated along the direction of tunnel growth ([010])
747 by varying degrees, but are of consistent width across the direction of tunnel growth
748 ([100]) over the entire duration of the reflux (from 6-10 nm wide after 6 hr (Fig. 3f) to ~8-
749 10 nm wide after 2 wk reflux (Fig. 3j)). These primary particles are then
750 crystallographically aligned and aggregated together across the direction of tunnel growth
751 via the OA of the [100] crystal faces to form secondary todorokite laths (Fig. 3e,g,i). Both
752 the length and width of these laths continues to increase with increasing reflux time (from
753 ~250x70 nm by 24 hr, to ~450x100 nm by 1 wk and ~750x100 nm by 2 wk reflux; Fig.
754 3e,g,i, respectively). These laths also become increasingly more crystalline (with notably
755 more defined lattice fringes at 2 wk reflux; Fig 3i,j), approximately commensurate with
756 the complete transformation of the birnessite precursor (occurring at some point between 1
757 wk and 2 wk reflux where at 2 wk reflux we cannot observe any 10 Å phyllomanganate or
758 phyllomanganate-like phase within the sample matrix; Fig 3i,j). These observations
759 indicate that the formation of secondary todorokite laths can be directly attributed to the
760 simultaneous growth from solution of primary todorokite crystallites along the [010]
761 direction, and their OA across the [100] direction, occurring primarily during the first
762 week of reflux, and that these laths undergo traditional crystal ripening, occurring over the
763 following weeks of reflux when all the precursor birnessite has been consumed. The
764 simultaneous occurrence of dissolution-recrystallisation and OA is expected in systems
765 that undergo growth via OA, although one growth mechanism may dominate at any given

766 time point (e.g., Waychunas et al., 2005; Kim et al., 2008). This nucleation and growth
767 process is entirely consistent with the nucleation, primary particle growth, and crystal
768 ripening stages proposed for our Ni-free system (Atkins et al., 2014).

769 Surface area and reaction solution pH (Table 3) also follow similar trends over the
770 course of the transformation to those observed in our Ni-free system and likely reflect the
771 fact that todorokite growth simultaneously involves both growth from solution and OA
772 (Atkins et al., 2014). In this regard, the relatively abrupt decrease in surface area over the
773 first week followed by its more gradual decline over the following 3 wk of reflux (Table
774 3; Figure 4) likely reflects the increase in todorokite particle size resulting from OA,
775 followed by a decrease in particle size occurring during the crystal ripening stage. On the
776 other hand, the slight increase in pH over the first week of reflux (Table 3) likely reflects a
777 release of hydroxyls into solution during birnessite dissolution (as expected during the
778 dissolution of (hydr)oxides), and may also reflect the loss of surface area resulting from
779 OA (where particle growth via aggregation (OA) and the associated loss of surface area is
780 reported to cause a net dehydroxylation effect (e.g., Kim et al., 2008)). The more
781 significant decrease in pH over the following 3 wk of reflux (Table 3) is approximately
782 concomitant with the final crystal ripening growth stage (beginning at some point between
783 1 wk and 2 wk reflux). As explained in our previous work, we are unlikely to have
784 captured this final growth stage in our Ni-free system (that ran over 72 hr; Atkins et al.,
785 2014). While very few studies investigate (hydr)oxide phase transformation and
786 subsequent crystal ripening, Kim et al. (2008) suggest that nanoparticle surface structural
787 rearrangements during ripening may result in a decrease in solution pH. The pH decrease
788 in our Ni-sorbed system, and to some extent the lack of pH decrease in our Ni-free system,
789 are certainly consistent with a ripening-induced pH decrease as suggested in the literature.

790 In summary, all of the above observations are consistent with our previous work
791 and indicate that our four-stage model for birnessite to todorokite transformation (Atkins
792 et al., 2014) is applicable to both Ni-free and Ni-sorbed phyllomanganates.

793

794 *4.1.2 Growth rate*

795 Although the presence of both structurally incorporated and surface adsorbed Ni
796 does not alter the growth mechanism of todorokite, we do see that this metal impurity
797 significantly slows the growth rate and reduces the crystallinity of this neo-formed phase,
798 compared to todorokite formed in our Ni-free system (Atkins et al., 2014). In contrast to
799 the Ni-free system, where characteristic todorokite XRD peaks are evident by 3 hr and

todorokite primary particles are observed with HR-TEM by 6 hr reflux (Atkins et al., 2014), here the appearance of characteristic todorokite XRD peaks is significantly delayed (only visible by 48 hr reflux (Fig. 2; where peaks may appear at any time point between the 24 and 48 hr scans)), and although primary particles are evident in the HR-TEM by 6 hr reflux, they comprise only a minor component of the overall sample matrix and are poorly crystalline (displaying only poorly defined lattice fringes (Fig. 3c,d)); both of which contribute to the early absence of todorokite peaks in the XRD spectra. Overall, the XRD and HR-TEM data at equivalent time points throughout the Ni-free and Ni-sorbed reflux show that todorokite formed in the Ni-sorbed system is only poorly crystalline (with significantly reduced intensity of the (001) and (002) reflections (XRD Fig. 2) and less well defined lattice fringes (HR-TEM Fig. 3c,d)). By 4 wk, despite the essentially complete transformation of our phyllomanganate to todorokite and 2-3 wk of crystal ripening (Fig. 3), the crystallinity of the neo-formed todorokite is still reduced (Fig. 2), compared to that formed by 72 hr reflux in the Ni-free system (Atkins et al., 2014).

In summary, it appears that the presence of ~1 wt% sorbed Ni has extended the timeframe required for the nucleation and growth of todorokite (from ~72 hr in the Ni-free to ~1 wk in the Ni-sorbed system) and significantly reduced the crystallinity of the neo-formed todorokite phase, even after an extended period of crystal ripening.

The reduction in todorokite growth rate in the Ni-sorbed system can be understood in light of our four-stage nucleation and growth mechanism for its formation (Atkins et al., 2014). Specifically, during the initial nucleation stage, thermally-induced kinking of the phyllomanganate layers is facilitated by the Jahn-Teller distortion of structural Mn(III) present in the 10 Å phyllomanganate (Cui et al., 2008; Bodeï et al., 2007; Atkins et al., 2014; Zhao et al., 2015), where moreover, the presence of sufficient structural Mn(III) is a prerequisite for todorokite formation (Atkins et al., 2014). Given the importance of structural Jahn-Teller distorted cations, we predict in our previous work that structurally incorporated cation impurities without Jahn-Teller distortion, such as Ni, should slow the transformation of birnessite to todorokite, by essentially slowing phyllomanganate layer kinking, thus slowing todorokite nucleation and the subsequent formation of todorokite primary particles (Atkins et al., 2014). Our results here, with ~0.6 wt% structurally incorporated Ni, confirm this prediction and can be attributed to a reduced rate of todorokite primary particle formation.

We show for the first time that, contrary to traditional understanding, the presence of sorbed Ni, at concentrations equivalent to those found in natural marine

ferromanganese precipitates, does not aid the transformation of birnessite to todorokite and in fact significantly slows todorokite formation and reduces todorokite crystallinity. Our results suggest that other cation impurities without Jahn-Teller distortion that structurally incorporate into birnessite (e.g., Co(III) (Manceau et al., 1997); Fe(III) (Yin et al., 2013)) will have a similar effect on todorokite formation and crystallinity, compared to todorokite formed in a relatively impurity-free system.

4.2 Mobility and Fate of Ni During the Transformation of Birnessite to Todorokite

4.2.1. Ni mobility and fate in experimental Ni-sorbed system

We also postulate in our previous work that structurally incorporated metal impurities might be lost to solution in order to facilitate the transformation process (Atkins et al., 2014). It is now clear that during the transformation of Ni-sorbed birnessite to todorokite, over the course of a 4 wk reflux, ~50 % of the initially sorbed Ni is released to solution (Table 1). Specifically, during the nucleation and growth stages, primarily occurring over first week of reflux, solid-associated Ni is sorbed to the phyllomanganate phase via surface and structurally incorporated complexes (HR-TEM EDS Table 2 and Ni EXAFS Fig. 6), despite the progressive formation of todorokite (XRD Fig. 2 and HR-TEM Fig. 3), and there is at least a 20 % release of Ni into solution (measured at 1 wk reflux; Table 1). During the final crystal ripening growth stage (beginning somewhere between 1 wk and 2 wk reflux), solid-associated Ni is sorbed to the todorokite as a surface adsorbed complex (observed at 2 wk reflux; Ni EXAFS Fig. 6), and, during the later stages of phyllomanganate transformation (occurring between 1 wk and 2 wk reflux) and the subsequent todorokite crystal ripening (beginning within this timeframe when all birnessite has been transformed), there is a ~50% release of Ni into solution (Table 1). Ultimately we see that in systems tending towards todorokite as the final transformation product, solid-associated Ni decreases by ~50 %.

It should be noted that our HR-TEM EDS data (Table 2), indicating that little if any Ni is associated with todorokite throughout the reflux, is not at odds with the fact we measure ~0.5 wt% Ni absolute Ni concentration in the todorokite product at 4 wk reflux (Table 1) because our EDS data cannot be interpreted as an absolute measurement of Ni associated with the phyllomanganate or todorokite (section 2.4). Our EDS data can only be interpreted to indicate that the todorokite forming throughout the reflux and present at the final 4 wk time point contains relatively less Ni than the phyllomanganate phase (section 3.1.2). In this sense the HR-TEM EDS data is consistent with a significant

868 decrease in solid-associated Ni as the reflux proceeds. It should also be noted that we do
869 not attribute the observed Ni release to the pH-induced desorption of the Ni surface
870 adsorbed onto our phyllomanganate and todorokite phases. While our experiments were
871 performed at a pH below circumneutral, which decreased over the duration of the reflux
872 (from a maximum pH of ~5.9 to a final pH of ~4.3; Table 3), our previous work shows
873 that significant Ni desorption from a birnessite of comparable crystallinity requires pH <
874 ~4 (Peacock and Sherman, 2007b). To our knowledge there is no published data on Ni
875 (de)sorption from todorokite, but its point of zero charge is similar to that for birnessite (at
876 pH ~3.5; e.g., Tan et al., 2008) and as such the pH-induced (de)sorption behaviour of Ni
877 will likely be similar, particularly given the fact that the molecular mechanism of Ni
878 adsorption to both birnessite and todorokite surfaces is also similar (involving tridentate
879 inner-sphere surface complexes (section 3.1.4.2)).
880
881 *4.2.2 Implications for Ni mobility and fate in marine sediments*
882 Our experimental system is designed to broadly replicate the diagenesis of
883 birnessite to todorokite in oxic marine sediments, using a reflux procedure that simulates
884 todorokite formation in natural environments (e.g., Feng et al., 2004), with an electrolyte
885 composition and concentration shown to best replicate the morphological and structural
886 features of natural marine todorokite (e.g., Cui et al., 2006). On the other hand, the pH of
887 our experimental system is lower than marine porewaters (circumneutral), yet work to date
888 suggests that an increase in pH is unlikely to significantly alter the mechanism of
889 todorokite nucleation and growth, or the fate of Ni during this process. In particular,
890 while the todorokite primary particles likely possess reduced surface charge (todorokite
891 pH_{PZC} ~3.5) in our experimental system compared to marine porewaters (perhaps
892 facilitating particle aggregation and thus OA-type growth; e.g., Banfield et al., 2000; Dale
893 et al., 2015), net particle surface charge in both systems should be negative (e.g., Tan et
894 al., 2008). As such, while the extent of OA might vary between our experiment and
895 marine porewaters, OA-type growth is still likely to be an important growth mechanism
896 for todorokite in marine sediments. Furthermore, the similarity in pH_{PZC} between
897 birnessite and todorokite indicates that the (de)sorption behaviour of these phases is likely
898 broadly similar, with Ni strongly adsorbed after pH ~4.5, and significantly different pH-
899 induced (de)sorption behaviour only occurring below pH ~4 (section 4.2.1). This
900 indicates that Ni (de)sorption behaviour at the pH of marine porewaters will not be

significantly different to that occurring in our experiment, such that our experimental system can be used as a broad proxy for Ni mobility and fate in oxic marine sediments.

Furthermore our analysis of natural marine ferromanganese deposits, as an analogue for ferromanganese (hydr)oxides dispersed in marine sediments and precipitated as discrete ferromanganese crusts and nodules, is consistent with our model mechanism for the transformation of birnessite to todorokite, and the resulting mobility and fate of Ni during this process. On the one hand, our experiments show that in Mn oxide precipitates that contain both phyllomanganate and todorokite, Ni is preferentially sorbed by the phyllomanganate phase, and as these precipitates become more todorokite rich, Ni is released into solution, leaving the neo-formed todorokite product depleted in Ni compared to the phyllomanganate precursor. Consistent with this, we find that in our natural hydrothermal sample containing both phyllomanganate and todorokite, the Ni associated with Mn oxides is indeed preferentially sorbed to the phyllomanganate phase, with no evidence for its surface adsorption or structural incorporation by the co-located todorokite (Fig. 8, 11). We also find that at the bulk scale our hydrothermal sample contains significantly less Ni (~0.07 wt.%) than our phyllomanganate-rich hydrogenetic and diagenetic samples (~0.4 and 0.5 wt.% Ni, respectively), while at the micro scale it is commonly reported for other natural intermixed ferromanganese precipitates that neo-formed todorokite typically contains substantially less Ni than its precursor 10 Å phyllomanganate (Siegel and Turner, 1983; Bodeï et al., 2007).

Overall our combined experimental and natural analyses are consistent with one another and indicate that in marine sediments where birnessite near-completely transforms to todorokite as the end product of diagenesis, at least half of the Ni originally sequestered to birnessite will be released to marine sedimentary porewaters. Furthermore, our results also show that the remaining solid-associated Ni will be adsorbed to neo-formed todorokite via surface complexation, as opposed to structural incorporation, and will therefore also be subject to remobilisation. Our work indicates that the marine diagenesis of birnessite likely provides a significant source of Ni to sedimentary porewaters and thus potentially a benthic flux of Ni to seawater.

5. SUMMARY AND CONCLUSIONS

We provide the first detailed understanding of the effect of sorbed Ni on the transformation of birnessite to todorokite in the marine environment, and the mobility and fate of this micronutrient during this diagenetic process. Specifically,

1. Sorbed Ni significantly slows the transformation of birnessite to todorokite and reduces the crystallinity of the neo-formed todorokite phase, but does not alter the mechanism and pathway of todorokite formation, compared to a Ni-free system. The inhibitory effect of sorbed Ni on todorokite formation can be attributed to a reduced rate of todorokite primary particle formation, where the presence of non Jahn-Teller distorted Ni within the phyllomanganate matrix is unfavourable for phyllomanganate layer kinking thus inhibiting todorokite nucleation and the subsequent formation of primary particles. The fact that sorbed Ni slows the transformation process is contrary to current knowledge, where it is understood that Ni should aid the transformation of birnessite to todorokite.
2. Sorbed Ni is released to solution during the transformation of birnessite to todorokite.
3. In systems tending towards todorokite as the final product of diagenesis, at least 50 % of the Ni originally sequestered by birnessite is released to solution, while the remaining solid-associated Ni is adsorbed to todorokite via surface complexation and is therefore also subject to remobilisation. Overall the marine diagenesis of birnessite likely provides a source of Ni to sedimentary porewaters and thus potentially provides a benthic flux of Ni to seawater.

Acknowledgements

We thank Michael Ward (Leeds Electron Microscopy and Spectroscopy Centre) for assistance with TEM imaging. We thank Diamond Light Source for access to beamlines B18 (grants SP7326, SP8045) and I20 (SP7325) which contributed to the results presented here. We also thank Andrew Dent, Giannantonio Cibin, Stephen Parry (beamline B18), and Fred Mosselmans and Tina Geraki (beamline I18) for support at Diamond Light Source. We thank Bob Knight (University of Hull) for ICP-OES analysis. We are indebted to Jim Hein (United States Geological Survey) for the provision of natural ferromanganese precipitate samples, and thank Bob Jones and John Ford (National Oceanography Centre, Southampton) for preparation of micro thin-sections. A. L. Atkins was supported via a NERC studentship. We finally thank 3 anonymous reviewers and the Associate Editor for their careful and thoughtful comments to improve the manuscript.

REFERENCES

Arrhenius G. (1963). Pelagic sediments. In: *Hill, M.N.* (Ed.), Sea, 3. Interscience, New York, pp 655–727.

Atkins A. L., Shaw S., Peacock C. L. (2014) Nucleation and growth of todorokite from birnessite: Implications for trace-metal cycling in marine sediments. *Geochim. Cosmochim. Acta.* **144**, 109-125.

Banerjee D. and Nesbitt H. W. (1999) Oxidation of aqueous Cr (III) at birnessite surfaces: constraints on reaction mechanism. *Geochim. Cosmochim. Acta.* **63**, 1671–1687.

Banfield J. F., Welch S. A., Zhang H., Ebert T. T. and Penn R. L. (2000) Aggregation-based crystal growth and microstructure development in natural iron oxyhydroxide biomineralization products. *Science.* **289**, 751–754.

Bargar J. R., Tebo B. M., Villinski J. E. (2000) In situ characterization of Mn (II) oxidation by spores of the marine Bacillus sp. strain SG-1. *Geochim. Cosmochim. Acta.* **64**, 2775–2778.

Bargar J. R., Tebo B. M., Bergmann U., Webb S. M., Glatzel P., Chiu V. Q. and Villalobos M. (2005) Biotic and abiotic products of Mn (II) oxidation by spores of the marine Bacillus sp. strain SG-1. *Am. Mineral.* **90**, 143–154.

Binsted N., Pack M. J., Weller M. T. and Evans J. (1996) Combined EXAFS and powder diffraction analysis. J. *Am. Chem. Soc.* 118, 10200–10210.

Binsted N. (1998) EXCURV98: The Manual. CLRC Daresbury Laboratory, Warrington, UK.

Bodeï S., Manceau A., Geoffroy N., Baronnet A., Buatier, M. (2007). Formation of todorokite from vernadite in Ni-rich hemipelagic sediments. *Geochim. Cosmochim. Acta* **71**, 5698–5716.

Booth C. H. and Hu Y.-J. (2009) Confirmation of standard error analysis techniques applied to EXAFS using simulations. *J. Phys.* 190, 1–6.

Brouwers G. J., Vijgenboom E., Corstjens P. L. A. M., De Vrind J. P. M., De Vrind-De Jong E. W. (2000): Bacterial Mn^{2+} Oxidizing Systems and Multicopper Oxidases: An Overview of Mechanisms and Functions. *Geomicrobiol. J.* **17:1**, 1-24.

Burns R. G. and Burns V. M. (1977) Mineralogy of ferromanganese nodules. In *Marine Manganese Deposits* (ed. G. P. Glasby). Elsevier, Amsterdam.

Burns V. M. and Burns R. G. (1978a) Authigenic todorokite and phillipsite inside

deep-sea manganese nodules. *Am. Mineral.* **63**, 827-831.

Burns V. M. and Burns R. G (1978b) Post-depositional metal enrichment processes inside manganese nodules from the north equatorial pacific. *Earth Planet. Sci. Lett.* **39**, 341-348.

Burns R. G. and Burns V. M. (1979) Manganese oxides. In: Burns R. G. (Ed.), *Marine Minerals. Rev. Mineral. Geochem.* 6. Mineralogy Society of America, Washington, DC, 1–46.

Burns R. G., Burns V. M. and Stockman H. (1983) A review of the todorokite buserite problem: implications to the mineralogy of marine manganese nodules. *Am. Mineral.* **68**, 972–980

Burns R. G., Burns V. M. and Stockman H. (1985) The todorokite–buserite problem: further consideration. *Am. Mineral.* **68**, 972–980

Burrows N. D., Hale C. R. H. and Penn R. L. (2012) Effect of ionic strength on the kinetics of crystal growth by orientated aggregation. *Cryst. Growth. Des.* **12**, 4787-797.

Cameron V., Vance D., Archer C. and House C. H. (2009) A biomarker based on the stable isotopes of Ni. *Proc. Natl. Acad. Sci. U.S.A.* **106**,10944-10948.

Cameron V. and Vance D. (2014) Heavy nickel isotope compositions in rivers and the oceans. *Geochim. Cosmochim. Acta.* **128**, 195-211.

Ching S., Krukowska K. S. and Suib S. L. (1999) A new synthetic route to todorokite-type manganese oxides. *Inorg. Chim. Acta* **294**, 123–132.

Chu N-C. (2004) An investigation into Hf and Fe isotopes in ferromanganese deposits and their applications to paleoceanography, p. 208. Ph.D. thesis, University of Southampton, UK.

Chukhrov F. V. and Gorshkov A. I. (1981) Iron and manganese oxide minerals in soils. *Trans. Royal Soc. Edinburgh, Earth Sci.* **72**, 195–200.

Cui H. J., Feng X. H., He J. Z., Tan W. F. and Liu F. (2006) Effects of reaction conditions on the formation of todorokite at atmospheric pressure. *Clays Clay Miner.* **54**, 605–615.

Cui H. J., Liu X. W., Tan W. F., Feng X. H., Liu F. and Ruan H. D. (2008) Influence of Mn(III) availability on the phase transformation from layered buserite to tunnel-structured todorokite. *Clays Clay Miner.* **56**, 397–403.

Cui H. J., Qiu G. H., Feng X. H., Tan W. F. and Liu F. (2009) Birnessites with

different average manganese oxidation states were synthesized, characterized, and transformed to todorokite at atmospheric pressure. *Clays Clay Miner*. **57**(6), 715–724.

Dale J. G., Stegemeier J. P. and Kim C. S. (2015) Aggregation of nanoscale iron oxyhydroxides and corresponding effects on metal uptake, retention, and speciation: I. Ionic-strength and pH. *Geochim. Cosmochim. Acta.* **148**, 100-112.

Dixon J. B. and Skinner H. C. W. (1992) Manganese minerals in surface environments. In: Skinner H. C. W. and Fitzpatrick R. W. (Eds), *Biomineralization Processes of Iron and Manganese: Modern and Ancient Environments*. Cremlingen: CATENA Verlag, 31–50.

Drits V. A., Silvester E., Gorshkov A. L., Manceau A., (1997) Structure of synthetic monoclinic Na-rich birnessite and hexagonal birnessite: I. Results from X-Ray Diffraction & Selected area electron diffraction. *Am. Mineral*. **82**, 946-961.

Feng Q., Kanoh H., Miyai Y. and Ooi K. (1995) Metal ion extraction/insertion reactions with todorokite-type manganese oxide in the aqueous phase. *Chem. Mater*. **7**, 1722–1727.

Feng Q., Yanagisawa K., Yamasaki N. (1998) Hydrothermal soft chemical process for synthesis of manganese oxides with tunnel structures. *J. Porous Mater*. **5**, 153-161.

Feng X. H., Tan W. F., Liu F., Wang J. B. and Ruan H. D. (2004) Synthesis of todorokite at atmospheric pressure. *Chem. Mater*. **16**, 4330–4336.

Feng X. H., Zhu M., Ginder-Vogel M., Ni C., Parikh S. J., Sparks D. L. (2010). Formation of nano-crystalline todorokite from biogenic Mn oxides. *Geochim. Cosmochim. Acta* **74**, 3232–3245.

Francis C. A., Co E. M., Tebo B. M. (2001). Enzymatic manganese (II) oxidation by a marine alpha-proteobacterium. *Appl. Environ. Microbiol*. **67,** (9), 4024-4029.

Frandsen C., Legg. B. L., Comolli. L. R., Zhang H., Gilbert B., Johnson E. and Banfield J. F. (2014) Aggregation-induced growth and transformation of β-FeOOH nanorods to micron-sized α-Fe2O3 spindles. *Cryst. Eng. Comm*. **16**, 1451-1458.

Gall L., Williams H. M., Siebert C., Halliday A. N., Herrington R. J. and Hein J. R. (2013). Nickel isotopic compositions of ferromanganese crusts and the constancy of deep ocean inputs and continental weathering effects over the Cenozoic. *Earth. Planet. Sci. Lett*. **317**, 148-155.

Gilbert B., Zhang H., Huang F., Finnegan M. P., Waychunas G. A., Banfield J. F.

(2003) Special phase transformation and crystal growth pathways observed in nanoparticles. *Geochem. Trans.* **4,** 20-27.

Giovanoli R., Biirki P., Giuffredi M. and StummW. (1975) Layer Structured Manganese Oxide Hydroxides. IV. The Buserite Group; Structure Stabilization by Transition Elements. *Chimia*. **29**. 517-52.

Goldberg E. D. (1954) Marine geochemistry. I. Chemical scavengers of the sea. *J. Geol*. **62**, 249–265.

Golden D. C., Chen C. C. and Dixon J. B. (1987) Transformation of birnessite to buserite, todorokite and manganite under mild hydrothermal treatment. *Clays Clay miner*. **35**, 271-280.

Huang F., Zhang H and Banfield J. F (2003) The role of orientated attachment crystal growth in hydrothermal coarsening of Nano crystalline ZnS. *J. Phys. Chem. B.* **107**, 10470-10475.

Kim C. S., Brown G. E. and Rytuba J. J. (2000) Characterization and speciation of mercury-bearing mine wastes using X-ray absorption spectroscopy. *Sci. Tot. Environ*. **261**, 157–168.

Kim C. S., Lentini C. J., Waychunas G. A. (2008) Associations between iron oxyhydroxide nanoparticles growth and metal adsorption/structural incorporation. In Adsorption of Metals By *Geomedia II*: Variables, Mechanisms, and Model Applications, Barnett, M. (Ed.), Elsevier Academic Press, 478.

Konhauser K. O., Pecoits E., Lalonde S. V., Papineau D., Nisbet E. G., Barley M. E., Arndt N. T., Zahnle K. and Kamber B. S. (2009) Oceanic Ni depletion and a methanogen famine before the great oxidation event. *Nature*. **458**, 750-753.

Koschinsky A. and Halbach P. (1995) Sequential leaching of marine ferromanganese precipitates: genetic implications. *Geochim. Cosmochim. Acta*. **59**, 5113-5132.

Koschinsky A. and Hein J. R. (2003) Acquisition of elements from seawater by ferromanganese crusts: Solid phase associations and seawater speciation. *Marine Geol*. **198**, 331-351.

Liu Z. H., Kang L., Ooi K., Yoji M. and Feng Q. (2005) Studies on the formation of todorokite-type manganese oxide with different crystalline birnessites by Mg2+-templating reaction. *J. Colloid. Interf. Sci*. **285**, 239–246.

Luo J., Zhang Q., Huang A., Giraldo O. and Suib S. L. (1999) Double-aging method for preparation of stabilized Na-buserite and transformations to todorokites incorporated with various metals. *Inorg. Chem*. **38**, 6106–6113.

Malinger K. A., Laubernds K., Son Y. C., Suib S. L. (2004) Effects of Microwave Processing on Chemical, Physical, and Catalytic Properties of Todorokite-Type Manganese Oxides. *Chem. Mater.* **16**, 4296-4303.

Manceau A., Drits V. A., Silvester E., Bartoli C. and Lanson B. (1997) Structural mechanism of Co^{2+} oxidation by the phyllomanganate buserite. *Am. Mineral.* **82**, 1150-1175.

Manceau A., Marcus M. A. and Tamura N. (2002) Quantitative speciation of heavy metals in soils and sediments by synchrotron X-ray techniques. In *Rev. Min. Geochem.* **49**, 341–428.

Manceau A., Marcus M. A., Tamura N., Proux O., Geoffroy N., Lanson B. (2004) Natural speciation of Zn at the micrometer scale in a clayey soil using X-ray fluorescence, absorption and diffraction. *Geochim. Cosmochim. Acta.* **68**, 2467-2483.

Manceau A., Lanson M. and Geoffroy N. (2007a) Natural speciation of Ni, Zn, Ba and As in ferromanganese coatings on quartz using X-ray fluorescence, absorption and diffraction. *Geochim. Cosmochim. Acta* **71**, 95–128.

Manceau A., Kersten M., Marcus M. A., Geoffroy N. and Granina L. (2007b) Ba and Ni speciation in a nodule of binary Mn oxide phase composition from Lake Bikal. *Geochim. Cosmochim. Acta* **71**, 1967–1981.

Moon E. M. and Peacock C. L. (2012) Adsorption of Cu(II) to ferrihydrite and ferrihydrite-bacteria composites: Importance of the carboxyl group for Cu mobility in natural environments, *Geochim. Cosmochim. Acta.* **92**, 203-219.

Pakarinen J., Koivula R., Laatikainen M., Laatikainen K., Paatero E., Harjula R. (2010) Nanoporous manganese oxides as environmental protective materials-Effect of Ca and Mg on metals sorption. *J. Hazard. Mater.* **180**, 234-240.

Peacock C. L. and Sherman D. M. (2007a) The crystal chemistry of Ni in marine ferromanganese crusts and nodules. *Am Mineral.* **92**, 1087-1097.

Peacock C. L. and Sherman D. M. (2007b) Sorption of Ni by birnessite: equilibrium controls on Ni in seawater. *Chem. Geol.* **238**, 94–106

Peacock C. L. (2009) Physiochemical controls on the crystal chemistry of Ni in birnessite: genetic implications for ferromanganese precipitates. *Geochim. Cosmochim. Acta* **73**, 3568–3578.

Peacock C. L. and Moon E. M. (2012) Oxidative scavenging of thallium by birnessite:

Explanation for thallium enrichment and stable isotope fractionation in marine ferromanganese precipitates. *Geochim. Cosmochim. Acta* **84**, 297-313.

Peña J., Kwon K. D., Refson K., Bargar J. R., Sposito G. (2010) Mechanisms of Ni sorption by bacteriogenic birnessite. *Geochim. Cosmochim. Acta* **74,** 3076-3089.

Penn R. L. and Banfield J. F. (1998a) Imperfect Orientated Attachment: Dislocation Generation in Defect-Free Nanocrystals. *Science*. **281**, 969-971.

Penn R. L. and Banfield J. F. (1998b) Orientated attachment and growth, twinning, polytypism, and formation of metastable phases: Insights from nanocrystalline TiO_2. *Am Mineral*. **83**, 1077-1082.

Penn R. L. and Banfield J. F. (1999) Morphology development and crystal growth in nanocrystalline aggregates under hydrothermal conditions: Insights from titania. *Geochim. Cosmochim. Acta*.**63**, 1549-1557.

Portehault D., Cassaignon S., Baudrin E. and Jolivet J. P. (2007) Morphology Control of Cryptomelane Type MnO_2 Nanowires by Soft Chemistry. Growth Mechanisms in Aqueous Medium. *Chem Mater*. **19**, 540-5417.

Post J. E. and Bish D. L. (1988) Rietveld refinement of the todorokite structure. *Am. Mineral*. **73**, 861–869.

Post J. E. and Veblen D. R. (1990) Crystal structure determinations of synthetic sodium, magnesium, and potassium birnessite using TEM and the Rietveld method. *Am. Mineral*. **75**, 477-489.

Post J. E. (1999) Manganese oxide minerals: crystal structures and economic and environmental significance. *Proc. Natl. Acad. Sci. U. S. A*. **96**, 3447–3454.

Post J. E., Heaney P. J. and Hanson J. (2003) Synchrotron X-ray diffraction study of the structure and dehydration behaviour of todorokite. *Am. Mineral*. **88**, 142-150.

Ravel B. and Newville M. (2005) ATHENA, ARTEMIS, HEPHAESTUS: Data analysis for X-ray absorption spectroscopy using IFEFFIT. *J. Synchrotron Radiat*. **12**, 537-541.

Ravel B. (2009) ATHENA Users' Guide, version 1.5. http://cars9.uchicago.edu/~ravel/software/doc/Athena/html/athena.pdf.

Rehkämper M., Frank M., Hein J. R., Porcelli D., Halliday A., Ingri J. and Liebetrau V. (2002) Thallium isotope variations in seawater and hydrogenetic, diagenetic, and hydrothermal ferromanganese deposits. *Earth Planet. Sci. Let*. **197**, 65–81.

Saratovsky I., Wightman P. G., Pasten P. A., Gaillard J. F. and Poeppelmeier K. R.

(2006) Manganese oxides: parallels between abiotic and biotic structures. *J. Am. Chem. Soc.* **128**, 11188–11198.

Scheinost A. C., Abend S., Pandya K. I. and Sparks D. L. (2001) Kinetic Controls on Cu and Pb Sorption by Ferrihydrite. *Environ. Sci. Technol.* **35,** 1090-1096.

Shen Y. F., Zerger R. P., DeGuzman R. N., Suib S. L., McCurdy L., Potter D. I. and O'Young C. L. (1993) Manganese oxide octahedral molecular sieves: preparation, characterization and application. *Science*. **260**, 511–515.

Siegel M. D. and Turner S. (1983) Crystalline todorokite associated with biogenic debris in manganese nodules. *Science*. **219**, 172-174.

Spiro T. G., Barger, J. R., Sposito, G., Tebo, B. M. (2010) Bacteriogenic manganese oxides. *Acc. Chem. Res.* **43**, 2-9.

Stern E. A. (1993) Number of relevant independent points in X-ray absorption fine-structure spectra. Phys. Rev. B 48, 9825–9827.

Takematsu N., Sato Y. and Okabe S. (1984) The formation of todorokite and birnessite in seawater pumped from underground. *Geochim. Cosmochim. Acta.* **48**, 1099-1106.

Tan W. F., Lu S. J., Liu F., Feng X. H., He J. Z., Koopall L. K. (2008) Determination of the point-of-zero charge of manganese oxides with different methods including an improved salt titration method. *Soil. Sci.* **173**, 277-286.

Tebo B. M., Johnson H. A., McCarthy J. K., Templeton A. S. (2005) Geomicrobiology of manganese (II) oxidation. *Trends Microbiol.* **13,** No.9, 421-428.

Tian Z. H., Yin Y. G., Suib S. L. (1997) Effect of Mg2+ Ions on the Formation of Todorokite Type Manganese Oxide Octahedral Molecular Sieves. *Chem. Mater.* **9**, 1126-1133.

Tomic S., Searle B. G., Wander A., Harrison N. M., Dent A. J., Mosselmans J. F. W., Inglesfield J. E. (2005) New Tools for the analysis of EXAFS: The DL EXCURV Package. CCLRC Technical Report DL-TR-2005-001. Council for the Central Laboratory of the Reasearch Councils, Swindon, UK.

Usui A. (1979) Nickel and copper accumulation as essential elements in 10Å manganite of deep-sea manganese nodules. *Nature*. **279**, 411-413.

Usui A and Terashima S. (1997) Deposition of Hydrogenetic and Hydrothermal Manganese Minerals in the Ogasawara (Bonin) Arc Area, Northwest Pacific. *Mar. Georesour. Geotech.* **15**, 127-154.

Van Driessche A. E. S., Benning L. G., Rodriguez-Blanco J. D., Ossorio M., Bots P.,

Garcia-Ruiz J.M. (2012) The role and implications of bassenite as a stable precursor phase to gypsum precipitation. *Science*. **336**, 69-72.

Vileno E., Ma Y., Zhou H., Suib S. L. (1998). Facile synthesis of synthetic todorokite OMS-1), co-precipitation reactions in the presence of a microwave field. *Micropor*. *Mesopor*. *Mat*. **70,** 3-15.

Villalobos M., Toner B., Bargar J. and Sposito G. (2003) Characterization of the manganese oxide produced by Pseudomonas putida strain MnB1. *Geochim*. *Cosmochim*. Acta **67**, 2649–2662.

Villalobos M., Lanson B., Manceau A., Toner B. and Sposito G. (2006) Structural model for the biogenic Mn oxide produced by Pseudomonas putida. *Am*. *Mineral*. **91**, 489–502.

Waychunas G. A, Kim C. S and Banfield J. F. (2005) Nanoparticulate iron oxide minerals in soils and sediments: unique properties and contaminant scavenging mechanisms. *J*. *Nanopart*. *Res*. **7**, 409-433.

Webb S. M., Tebo B. M. and Bargar J. R. (2005a) Structural characterization of biogenic manganese oxides produced in seawater by the marine Bacillus sp. strain SG-1. *Am*. *Mineral*. **90**, 1342–1357.

Webb S. M., Dick G. J., Bargar J. R. and Tebo B .M. (2005b) Evidence for the presence of Mn(III) intermediates in the bacterial oxidation of Mn(II). *P*. *NATL*. *ACAD*. *SCI*. *U*. *S*. *A*. **102**, 6. 5558-5563.

Xu Y., Axe L., Boonfueng T., Tyson T. A., Trivedi P. and Pandya K. (2007) Ni(II) complexation to amorphous hydrous ferric oxide: An X-ray absorption spectroscopy study. *J*. *Coll*. *Inter*. *Sci*. **314**, 10-17.

Yin H., Liu F., Feng X., Hub T., Zheng L., Qiu G., Koopal L. K. and Tan W. (2013) Effects of Fe doping on the structures and properties of hexagonal birnessites - Comparison with Co and Ni doping. *Geochim*. *Cosmochim*. *Acta*. **117**, 1-15.

Zhao H. Y, Liang X. R, Yin H., Liu F., Tan W. F, Qiu G. H, Feng X. H. (2015) Formation of todorokite from "*c*-disordered" H+-birnessites: the roles of average manganese oxidation state and interlayer cations. *Geochem*. *Trans*. **16**, 8.

1230 **TABLES**

1231 **Table 1:** Absolute Ni concentrations for our birnessite precursor, 10 Å phyllomanganate
1232 intermediate and reflux products.

1233

Sample	wt% Ni[a]
Birnessite	0.92±0.002
10Å phyllomanganate	1.03±0.005
3hr reflux	0.96±0.007
6hr reflux	1.07±0.010
12hr reflux	1.00±0.004
24hr reflux	1.04±0.003
48hr reflux	0.99±0.009
72hr reflux	0.98±0.010
1wk reflux	0.80±0.011
4wk reflux	0.54±0.003

1234 [a]Error is standard deviation of 3
1235 measurements made on separate solid
1236 aliquots.

1237

1238 **Table 2:** HR-TEM EDS data for EDS spot measurements made on a selection of our
1239 reflux products. Positions of spot analyses are shown on Figure 3. Numbers in parentheses
1240 below the measured values are the errors given as the standard deviation of triplicate
1241 measurements for each spot.

1242

Sample	Cu (wt%)	C (wt%)	Mn (wt%)	O (wt%)	Mg (wt%)	Ni (wt%)	Sum (wt%)
6 hr EDS (1)	50.7 (0.7)	21.1 (0.8)	16.3 (0.4)	10.9 (0.6)	0.7 (0.1)	0.4 (0.1)	100.1
6 hr EDS (2)	51.9 (0.8)	25.9 (0.8)	12.5 (0.4)	8.9 (0.5)	0.7 (0.1)	0	99.9
24 hr EDS (1)	26.8 (0.4)	0	41.4 (0.5)	28.9 (0.6)	2.0 (0.1)	1.0 (0.1)	100.1
24 hr EDS (2)	22.3 (0.3)	0	35.5 (0.4)	39.5 (0.5)	2.6 (0.1)	0	99.9
1 wk EDS (1)	32.4 (0.5)	0	34.4 (0.5)	30.1 (0.7)	2.2 (0.2)	0.9 (0.1)	100
1 wk EDS (2)	37.0 (0.6)	4.6 (0.5)	31.5 (0.6)	25.3 (0.7)	1.7 (0.2)	0	100.1
2 wk EDS	31.8 (0.4)	14.0 (0.5)	28.4 (0.4)	24.2 (0.5)	1.7 (0.1)	0	100.1

1243

1244 **TABLE 3:** Specific surface area of the solid products, and Ni and Mn concentrations and
1245 pH of the reflux solutions for the 10 Å phyllomanganate intermediate (time 0) and
1246 subsequent reflux products.
1247

Sample	Surface Area[a] (m^2/g)	Ni[b] (mM)	Mn[b] (mM)	pH[c]
10Å phyllomanganate	102.3	N/A	N/A	N/A
3hr reflux	84	$0.004 \pm 8.1\times10^{-5}$	$0.003 \pm 3.8\times10^{-5}$	5.29
6hr reflux	88	$0.006 \pm 5.2\times10^{-4}$	$0.017 \pm 4.2\times10^{-4}$	5.47
12hr reflux	87	$0.007 \pm 8.1\times10^{-4}$	$0.019 \pm 6.5\times10^{-4}$	5.49
24hr reflux	97	$0.010 \pm 2.2\times10^{-4}$	$0.018 \pm 3.3\times10^{-4}$	5.56
48hr reflux	99	$0.021 \pm 3.9\times10^{-4}$	$0.010 \pm 3.2\times10^{-4}$	5.93
72hr reflux	95	$0.030 \pm 5.7\times10^{-4}$	$0.008 \pm 2.1\times10^{-4}$	5.95
5day reflux	84	$0.042 \pm 9.6\times10^{-4}$	$0.009 \pm 3.3\times10^{-4}$	5.82
1wk reflux	37	$0.054 \pm 1.1\times10^{-3}$	$0.008 \pm 1.9\times10^{-4}$	5.81
4wk reflux	20	$0.093 \pm 3.8\times10^{-4}$	$0.002 \pm 5.6\times10^{-3}$	4.26

1248 [a]All surface area measurements are ±5%. [b]All reported errors are the standard deviation as
1249 determined from triplicate measurements. [c]All pH measurements are ± 0.05 pH units.
1250

1251

1252 **TABLE 4:** EXAFS fits for Ni sorbed and incorporated reference compounds, fit by
1253 refinement of a single model cluster.
1254

Shell	*N*	*R* (Å)	$2\sigma^2$ ($Å^2$)	*θ*	*φ*	EF	R (%)	Reduced Chi^2
Ni-structurally incorporated natural birnessite (Ni-birnessite^S)								
Ni_0	*1.0*	0.00	0.000	*0*	*0*	1.43	18.1	17.6
O_1	*3.0*	2.01	0.012	*47*	*0*			
O_2	*3.0*	2.04	0.011	*136*	*180*			
Mn_3	*3.0*	2.88	0.012	*90*	*270*			
Mn_4	*3.0*	2.85	0.013	*90*	*90*			
Mn_5	*3.0*	5.94	0.006	*90*	*270*			
Mn_6	*3.0*	4.94	0.010	*90*	*180*			
Mn_7	*3.0*	5.05	0.012	*90*	*0*			
Mn_8	*3.0*	5.90	0.005	*90*	*90*			
O_9	*3.0*	3.33	0.016	*105*	*0*			
O_{10}	*3.0*	3.58	0.009	*75*	*180*			
O_{11}	*3.0*	4.47	0.006	*75*	*100*			
O_{12}	*3.0*	4.45	0.009	*105*	*45*			
O_{13}	*3.0*	4.51	0.004	*100*	*80*			
O_{14}	*3.0*	4.65	0.011	*75*	*135*			

Ni-sorbed c-disordered birnessite 24 hr (Ni-birnessite^{V})								
Ni_0	*1.0*	0.00	0.000	*0*	*0*	3.45	13.9	10.4
O_1	*3.0*	2.08	0.011	*60*	*270*			
O_2	*3.0*	2.01	0.010	*120*	*90*			
O_3	*3.0*	3.26	0.004	*150*	*270*			
Mn_4	*3.0*	3.53	0.005	*125*	*0*			
Mn_5	*3.0*	3.42	0.004	*126*	*180*			
O_6	*3.0*	4.35	0.004	*136*	*90*			
O_7	*3.0*	3.61	0.005	*110*	*270*			
Mn_8	*3.0*	5.38	0.004	*110*	*90*			
Mn_9	*3.0*	5.54	0.005	*110*	*270*			
Mn_{10}	*3.0*	6.01	0.004	*110*	*0*			
Mn_{11}	*3.0*	5.82	0.004	*110*	*180*			
Ni-sorbed todorokite 24 hr (Ni-todorokite_24hr)								
Ni_0	*1.0*	0.00	0.000	*0*	*0*	-1.15	19.6	14.6
O_1	*1.0*	2.05	0.010	94	358			
O_2	*1.0*	2.00	0.011	*90*	*180*			
O_3	*1.0*	2.06	0.012	*90*	*90*			
O_4	*1.0*	2.06	0.010	*90*	272			
O_5	*1.0*	2.10	0.007	*0*	*0*			
O_6	*1.0*	2.03	0.007	176	*0*			
Mn_7	*1.0*	3.00	0.012	*90*	*315*			
Mn_8	*1.0*	3.10	0.009	*135*	*0*			
Ni-sorbed todorokite 1 wk (Ni-todorokite_1wk)								
Ni_0	*1.0*	0.00	0.000	*0*	*0*	0.68	20.4	15.8
O_1	*1.0*	2.05	0.010	94	358			
O_2	*1.0*	2.00	0.011	*90*	*180*			
O_3	*1.0*	2.06	0.013	*90*	*90*			
O_4	*1.0*	2.06	0.011	*90*	272			
O_5	*1.0*	2.11	0.007	*0*	*0*			
O_6	*1.0*	2.03	0.008	176	*0*			
Mn_7	*1.0*	2.98	0.011	*90*	*315*			
Mn_8	*1.0*	3.10	0.007	*135*	*0*			

N is the number of atoms in a shell. *R*, θ and φ are the interatomic distance and spherical coordinates of the prototype atom in each shell with either C_1 or C_3 symmetry. $2\sigma^2$ is the Debye–Waller factor. EF is the correction to the Fermi energy value assigned in ATHENA. Values in italics were held constant during refinement.

TABLE 5: EXAFS fits for our birnessite precursor, 10 Å phyllomanganate intermediate and all reflux products.

a) Samples fit by linear combination of reference spectra.

Sample	**EF**	***N* Ni^S**	***N* Ni^V**	**R (%)**	**Reduced Chi^2**
Birnessite	3.46	0.46±0.04	0.54±0.04	23.3	2.9
10Å phyllomanganate	0.51	0.62±0.04	0.38±0.04	21.3	2.2
3 hr reflux	2.43	0.58±0.04	0.42±0.04	22.5	2.6
6 hr reflux	1.81	0.59±0.04	0.41±0.04	21.5	2.2
12 hr reflux	0.62	0.62±0.04	0.39±0.04	21.6	2.1
24 hr reflux	2.13	0.70±0.05	0.30±0.05	24.4	2.7
48 hr reflux	2.21	0.65±0.04	0.35±0.04	23.5	2.7
72 hr reflux	1.80	0.61±0.04	0.39±0.04	23.4	2.5
5 day reflux	0.83	0.59±0.04	0.41±0.04	22.1	2.2
1 wk reflux	1.44	0.62±0.04	0.38±0.04	23.3	2.5

EF is the correction to the Fermi energy value assigned in ATHENA. *N* Ni^S is the number of Ni atoms (Ni site occupancy) for reference spectrum Ni-structurally incorporated natural birnessite (Ni-birnessite^S). *N* Ni^V is the number of Ni atoms (Ni site occupancy) for reference spectrum Ni-sorbed c-disordered birnessite (Ni-birnessite^V).

TABLE 5: EXAFS fits for our birnessite precursor, 10 Å phyllomanganate intermediate and all reflux products.

b) Samples fit by refinement of a single model cluster.

Shell	***N***	***R* (Å)**	**$2\sigma^2$ (Å^2)**	***θ***	***φ***	**EF**	**R (%)**	**Reduced Chi^2**
2 wk reflux								
Ni_0	*1.0*	0.00	0.000	*0*	*0*	0.10	20.1	13.5
O_1	*1.0*	1.98	0.005	*94*	*358*			
O_2	*1.0*	2.06	0.011	*90*	*180*			
O_3	*1.0*	2.10	0.012	*90*	*90*			
O_4	*1.0*	2.09	0.011	*90*	*272*			
O_5	*1.0*	2.04	0.011	*0*	*0*			
O_6	*1.0*	2.05	0.007	*176*	*0*			
Mn_7	*1.0*	2.95	0.011	*90*	*315*			
Mn_8	*1.0*	3.11	0.009	*135*	*0*			
4 wk reflux								
Ni_0	*1.0*	0.00	0.000	*0*	*0*	2.15	13.7	8.1
O_1	*1.0*	1.98	0.005	*94*	*358*			
O_2	*1.0*	2.06	0.012	*90*	*180*			
O_3	*1.0*	2.05	0.013	*90*	*90*			
O_4	*1.0*	2.10	0.012	*90*	*272*			
O_5	*1.0*	2.06	0.012	*0*	*0*			
O_6	*1.0*	2.05	0.007	*176*	*0*			
Mn_7	*1.0*	2.94	0.013	*90*	*315*			
Mn_8	*1.0*	3.11	0.008	*135*	*0*			

N is the number of atoms in a shell. *R*, *θ* and *φ* are the interatomic distance and spherical coordinates of the prototype atom in each shell with either C_1 or C_3 symmetry. $2\sigma^2$ is the Debye–Waller factor. EF is the correction to the Fermi energy value assigned in ATHENA. Values in italics were held constant during refinement.

TABLE 6: EXAFS fits for natural ferromanganese samples, fit by refinement of a single model cluster.

Shell	***N***	***R*** **(Å)**	**2σ^2 (Å^2)**	***θ***	***φ***	**EF**	**R (%)**	**Reduced Chi^2**
HG_FeMn								
Ni_0	*1.0*	0.00	0.000	*0*	*0*	2.34	25.2	29.0
O_1	*3.0*	2.02	0.012	*47*	*0*			
O_2	*3.0*	2.08	0.011	*136*	*180*			
Mn_3	*3.0*	2.93	0.015	*90*	*270*			
Mn_4	*3.0*	2.85	0.012	*90*	*90*			
Mn_5	*3.0*	5.99	0.010	*90*	*270*			
Mn_6	*3.0*	4.96	0.011	*90*	*180*			
Mn_7	*3.0*	5.08	0.010	*90*	*0*			
Mn_8	*3.0*	5.88	0.009	*90*	*90*			
O_9	*3.0*	3.31	0.010	*105*	*0*			
O_{10}	*3.0*	3.53	0.010	*75*	*180*			
O_{11}	*3.0*	4.52	0.008	*75*	*100*			
O_{12}	*3.0*	4.45	0.010	*105*	*45*			
O_{13}	*3.0*	4.55	0.010	*100*	*80*			
O_{14}	*3.0*	4.65	0.013	*75*	*135*			
DG_FeMn								
Ni_0	*1.0*	0.00	0.000	*0*	*0*	1.30	20.8	22.7
O_1	*3.0*	2.04	0.015	*47*	*0*			
O_2	*3.0*	2.06	0.009	*136*	*180*			
Mn_3	*3.0*	2.86	0.015	*90*	*270*			
Mn_4	*3.0*	2.90	0.017	*90*	*90*			
Mn_5	*3.0*	6.00	0.009	*90*	*270*			
Mn_6	*3.0*	4.95	0.014	*90*	*180*			
Mn_7	*3.0*	5.08	0.010	*90*	*0*			
Mn_8	*3.0*	5.89	0.009	*90*	*90*			
O_9	*3.0*	3.30	0.009	*105*	*0*			
O_{10}	*3.0*	3.49	0.013	*75*	*180*			
O_{11}	*3.0*	4.54	0.008	*75*	*100*			
O_{12}	*3.0*	4.42	0.011	*105*	*45*			
O_{13}	*3.0*	4.57	0.009	*100*	*80*			
O_{14}	*3.0*	4.64	0.013	*75*	*135*			
HT_FeMn								
Ni_0	*1.0*	0.00	0.000	*0*	*0*	3.14	24.3	27.4
O_1	*3.0*	2.01	0.010	*47*	*0*			
O_2	*3.0*	2.06	0.010	*136*	*180*			
Mn_3	*3.0*	2.94	0.018	*90*	*270*			
Mn_4	*3.0*	2.84	0.013	*90*	*90*			
Mn_5	*3.0*	6.00	0.011	*90*	*270*			
Mn_6	*3.0*	4.96	0.011	*90*	*180*			
Mn_7	*3.0*	5.09	0.010	*90*	*0*			
Mn_8	*3.0*	5.91	0.010	*90*	*90*			
O_9	*3.0*	3.36	0.014	*105*	*0*			

O_{10}	*3.0*	3.50	0.010	*75*	*180*			
O_{11}	*3.0*	4.49	0.012	*75*	*100*			
O_{12}	*3.0*	4.50	0.012	*105*	*45*			
O_{13}	*3.0*	4.55	0.012	*100*	*80*			
O_{14}	*3.0*	4.65	0.012	*75*	*135*			

N is the number of atoms in a shell. *R*, θ and φ are the interatomic distance and spherical coordinates of the prototype atom in each shell with either C_1 or C_3 symmetry. $2\sigma^2$ is the Debye–Waller factor. EF is the correction to the Fermi energy value assigned in ATHENA. Values in italics were held constant during refinement.

1287 **FIGURE CAPTIONS**

1288

1289 **FIGURE 1:** Molecular clusters used to model EXAFS spectra of (a) Ni surface adsorbed
1290 at Mn octahedral vacancy sites present in the layers of a hexagonal phyllomanganate, (b)
1291 Ni structurally incorporated into the layers of a phyllomanganate, and (c) Ni surface
1292 sorbed to todorokite as a tridentate corner-sharing complex.

1293

1294 **FIGURE 2**: X-ray diffraction patterns for our Ni-sorbed c-disordered birnessite precursor,
1295 Ni-sorbed 10 Å phyllomanganate intermediate and subsequent reflux products.
1296 Characteristic X-ray diffraction peaks are labeled for our c-disordered birnessite (B), 10 Å
1297 phyllomanganate intermediate (10Å P) and todorokite product (T) (based on Drits et al.,
1298 1997 for turbostratic birnessite, JCPDS-32-1128 for buserite and JCPDS-38-475 for
1299 todorokite, respectivley). The * symbol indicates residual $MgCl_2$.

1300

1301 **FIGURE 3:** Transmission electron micrographs of: (a-b) Ni-sorbed 10 Å
1302 phyllomanganate with image (a) highlighting the plate-like morphology and thick
1303 phyllomanganate layer edges, and (b) highlighting the phyllomanganate interlayer
1304 spacing. (c-d) Reflux product after 6 hr reflux, where (c) highlights the phyllomanganate
1305 dominated mineralogy of the sample matrix and (d) highlights the formation of poorly
1306 crystalline todorokite primary particles, elongated along the [010] direction and relatively
1307 uniform in size (6-10 nm) across the [100] direction. (e-f) Reflux product after 24 hr
1308 reflux where (e) highlights the mixed birnessite/todorokite mineralogy and (f) highlights
1309 the formation of poorly crystalline plate-like todorokite, and the formation of large
1310 secondary todorokite laths, formed via the lateral aggregation of todorokite primary
1311 particle building blocks. (g-h) Reflux product after 1 wk reflux, indicating that the
1312 mineralogy is largely dominated by todorokite. (i-j) Reflux product after 2 wk reflux
1313 where the red lines in (i) highlight the lateral aggregation of primary todorokite particles
1314 and (j) highlights the relatively uniform widths of the individual todorokite primary
1315 particles. Circles in images (c), (e), (g) and (i) indicate the position of EDS analysis, where
1316 the circle is approximately equal to the size of the analyzed area. Approximate wt % of Ni
1317 at the selected EDS points is shown in Table 1.

1318

1319 **FIGURE 4:** Surface area of the solid reflux products and the concentrations of Ni and Mn
1320 in the reflux solution as a function of reflux time. The first surface area measurement is

the Ni-sorbed 10 Å phyllomanganate intermediate at 0 hr reflux; measurements of Ni and Mn in the reaction solution start at 3 hr reflux. For exact values and error measurements see Table 3 (errors for BET are ±5% of the measured value and for [Mn] and [Ni] are smaller than the data points).

FIGURE 5: Ni K-edge EXAFS and Fourier transforms of the EXAFS for the reference compounds. Ni-birnessite^{S} is a Ni-incorporated natural poorly crystalline birnessite; Ni-birnessite^{V} is a synthetic c-disordered birnessite at 24 hr contact time with Ni sorbed at the Mn octahedral vacancy sites, Ni-todorokite_24hr and Ni-todorokite_1wk are synthetic todorokite samples at 24 hr and 1 wk contact times, respectively. Solid lines are data, dotted lines are fits.

FIGURE 6: Ni K-edge EXAFS and Fourier transforms of the EXAFS for the experimental samples including Ni-sorbed c-disordered birnessite precursor, Ni-sorbed 10 Å phyllomanganate intermediate and subsequent reflux products at 3, 6, 24 and 48 hr, and 1, 2 and 4 wk. Solid lines are data, dotted lines are fits.

FIGURE 7: Bulk powder X-ray diffraction patterns for (a) the hydrogenetic ferromanganese crust collected from the Pacific Ocean (b) the diagenetic ferromanganese nodule from the Pacific Ocean and (c) the hydrothermal deposit, collected from the Lau Basin. X-ray diffraction peaks are labeled for phyllomanganate (P) (based on JCPDS-15-604 for vernadite, Drits et al., 1997 for turbostratic birnessite and JCPDS-32-1128 for buserite) and todorokite (T) (based on JCPDS-38-475). ■ denotes hydroxyapatite ($Ca_5(PO_4)_3(OH)$), ● denotes quartz (based on JCPDS 9-0432 and 46-1045, respectively).

FIGURE 8: μ-XRF elemental maps showing the distribution of Mn (blue), Fe (green) and Ni (red) in (a-b) the hydrogenetic ferromanganese crust sample, (c-d) the diagenetic ferromanganese nodule and (e-f) the hydrothermal ferromanganese deposit. Pixel size is 10x10 μm, and total map area for the hydrogenetic sample is 1700x1700 μm, and for the diagenetic and hydrothermal samples is 400x400 μm. Points of interest (POI) subject to μ-EXAFS analysis are shown (white boxes are not to scale).

FIGURE 9: Scatter plots displaying normalized fluorescence counts between Mn-Fe, Ni-Mn, and Ni-Fe, for (a-c) the hydrogenetic ferromanganese crust sample, (d-f) the diagenetic ferromanganese nodule and (g-i) the hydrothermal ferromanganese deposit.

FIGURE 10: Mn K-edge EXAFS for the selected POI in the natural samples. The hydrogenetic, diagenetic and hydrothermal samples are labeled as HG_FeMn, DG_FeMn and HT_FeMn, respectively. Dashed vertical lines indicate key *k*-space indicator regions at ~6.7, 8 and 9.2 $Å^{-1}$.

FIGURE 11: Ni K-edge EXAFS and Fourier transforms of the EXAFS for the natural hydrogenetic, diagenetic and hydrothermal samples, labeled as HG_FeMn, DG_FeMn and HT_FeMn, respectively. Solid lines are data, dotted lines are fits.

Figure1

Atkins et al: Figure 1 (one column wide)

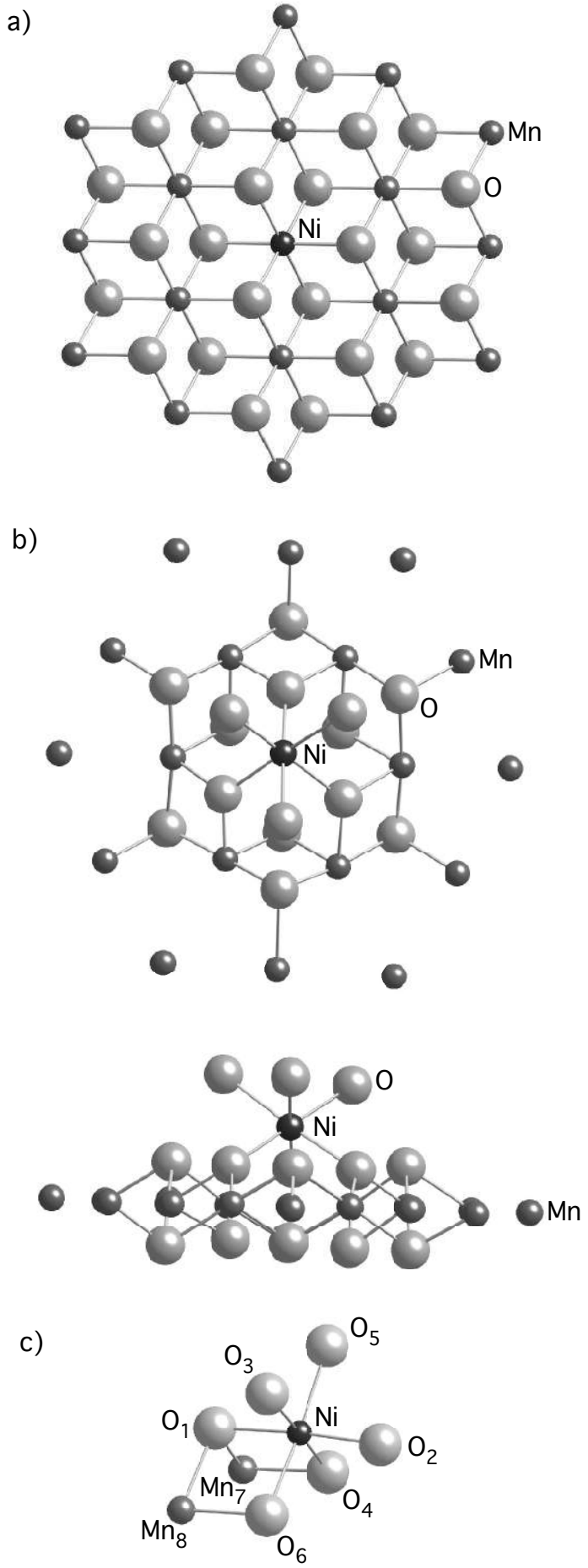

Figure2

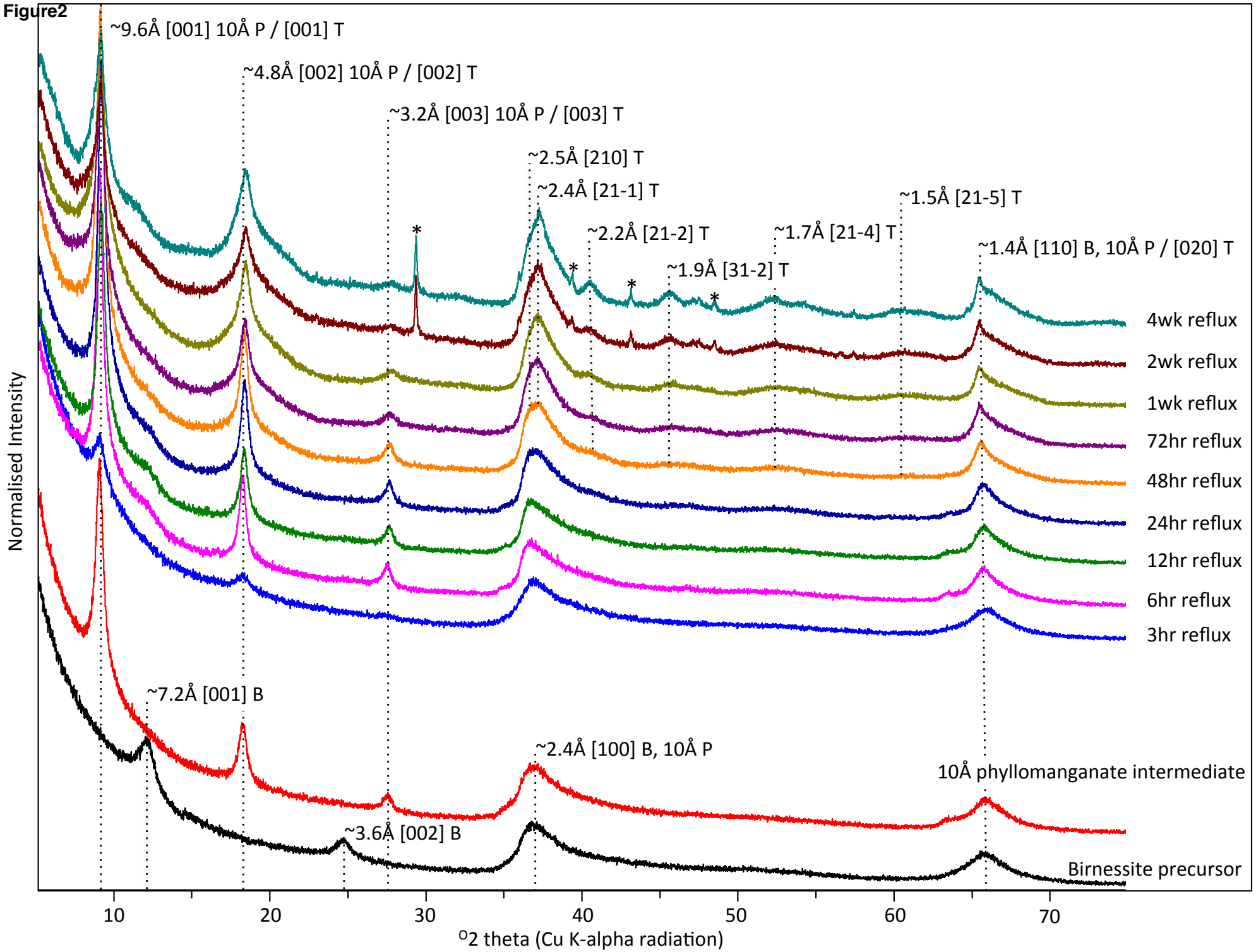
~9.6Å [001] 10Å P / [001] T
~4.8Å [002] 10Å P / [002] T
~3.2Å [003] 10Å P / [003] T
~2.5Å [210] T
~2.4Å [21-1] T
~2.2Å [21-2] T
~1.9Å [31-2] T
~1.7Å [21-4] T
~1.5Å [21-5] T
~1.4Å [110] B, 10Å P / [020] T
*
4wk reflux
2wk reflux
1wk reflux
72hr reflux
48hr reflux
24hr reflux
12hr reflux
6hr reflux
3hr reflux
~7.2Å [001] B
~2.4Å [100] B, 10Å P
10Å phyllomanganate intermediate
~3.6Å [002] B
Birnessite precursor
Normalised Intensity
10
20
30
40
50
60
70
°2 theta (Cu K-alpha radiation)

Figure3

Atkins et al: Figure 3 (two columns wide)

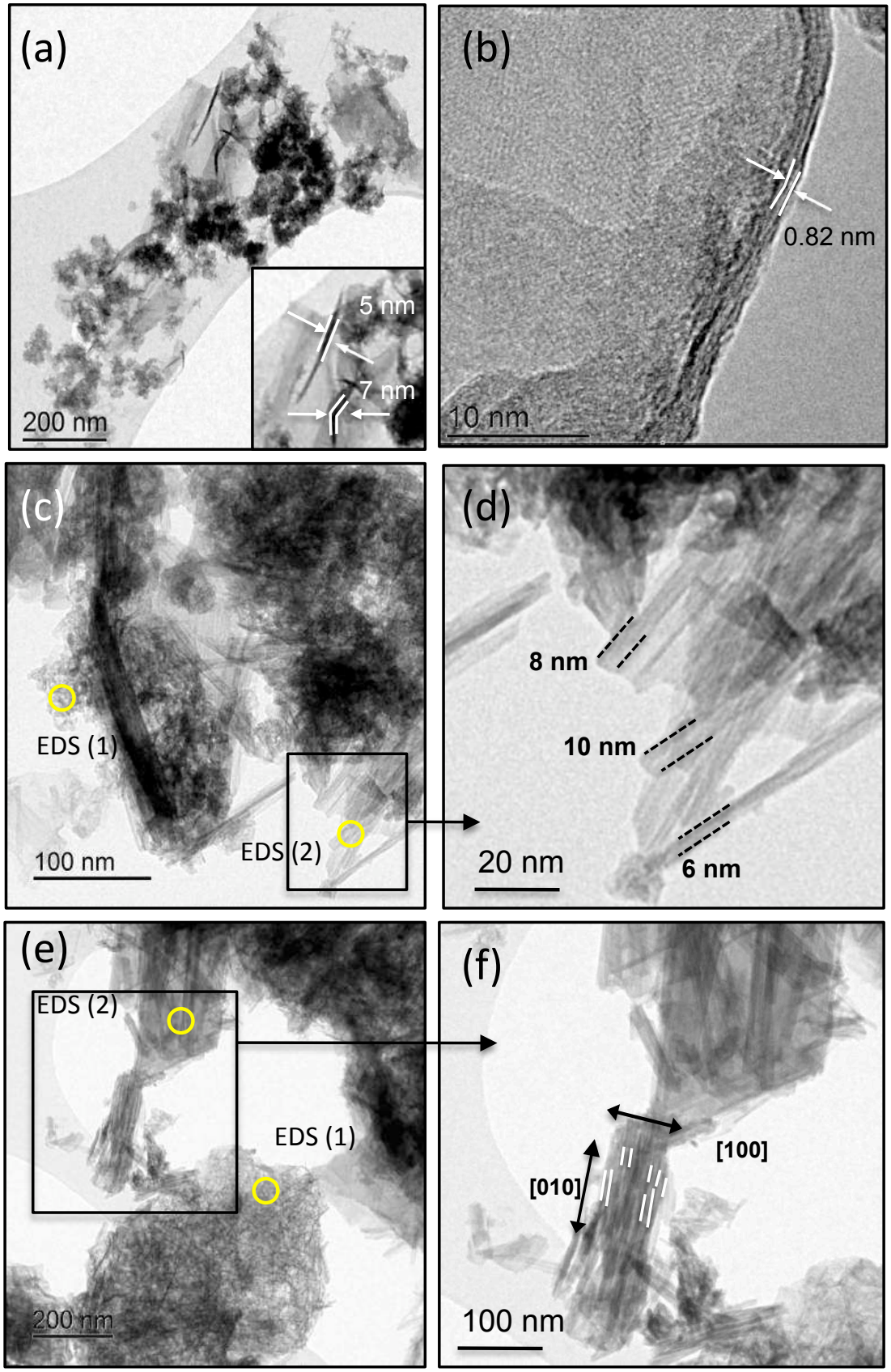

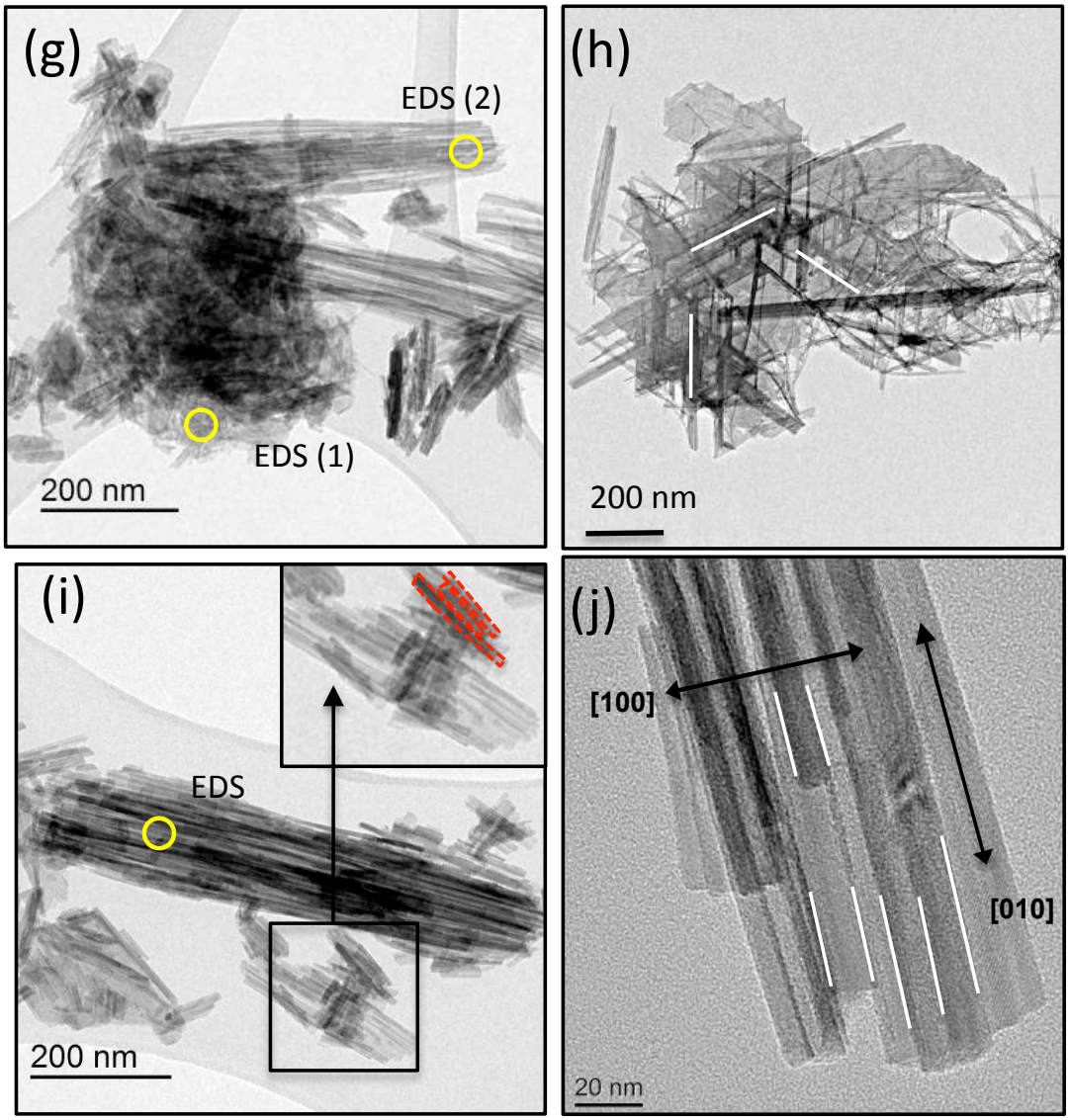
(g)
EDS (2)
EDS (1)
200 nm
(h)
200 nm
(i)
EDS
200 nm
(j)
[100]
[010]
20 nm

Figure 4

Atkins et al: Figure 4 (one column wide)

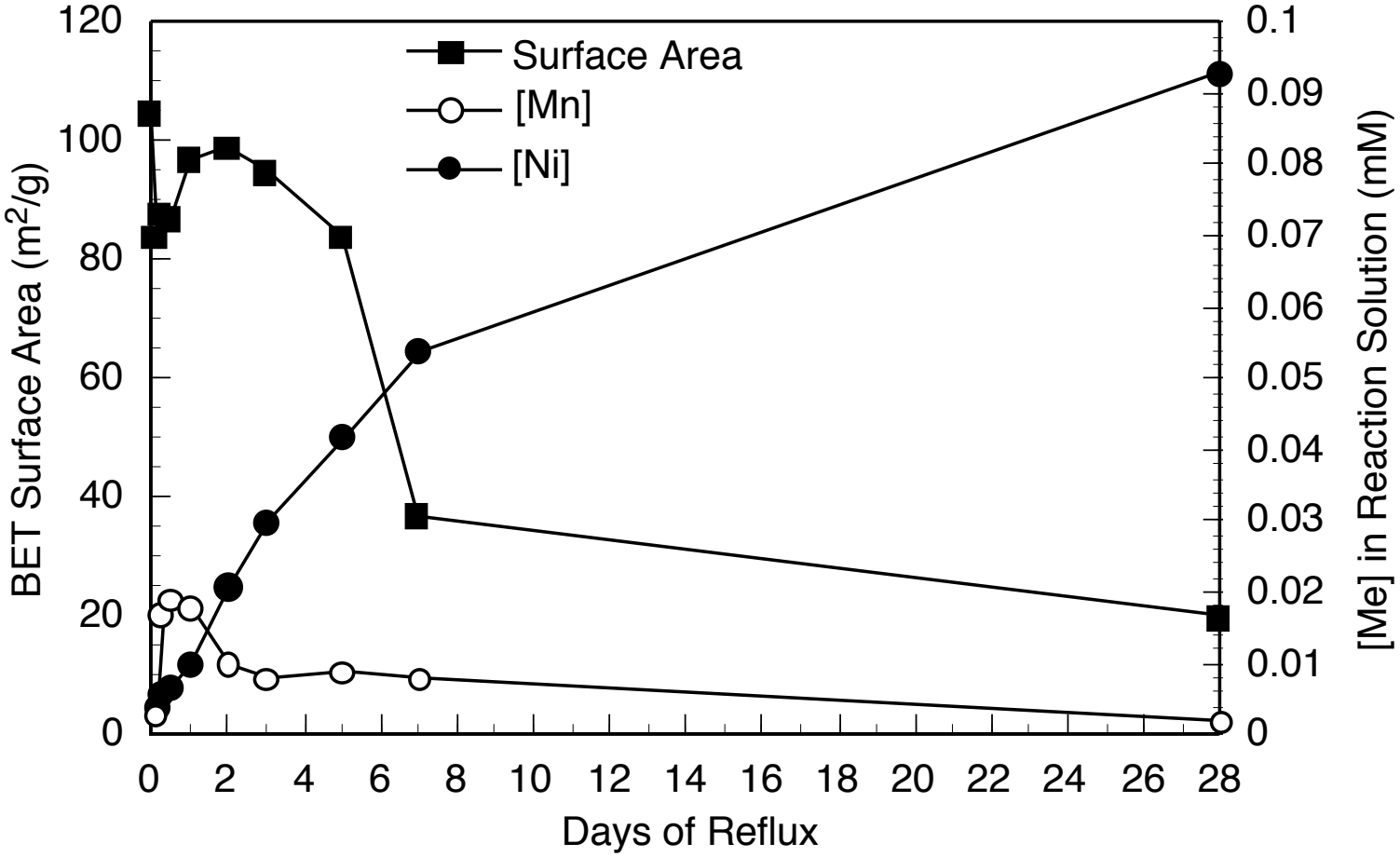

Figure 5 Atkins et al: Figure 5 (two columns wide)

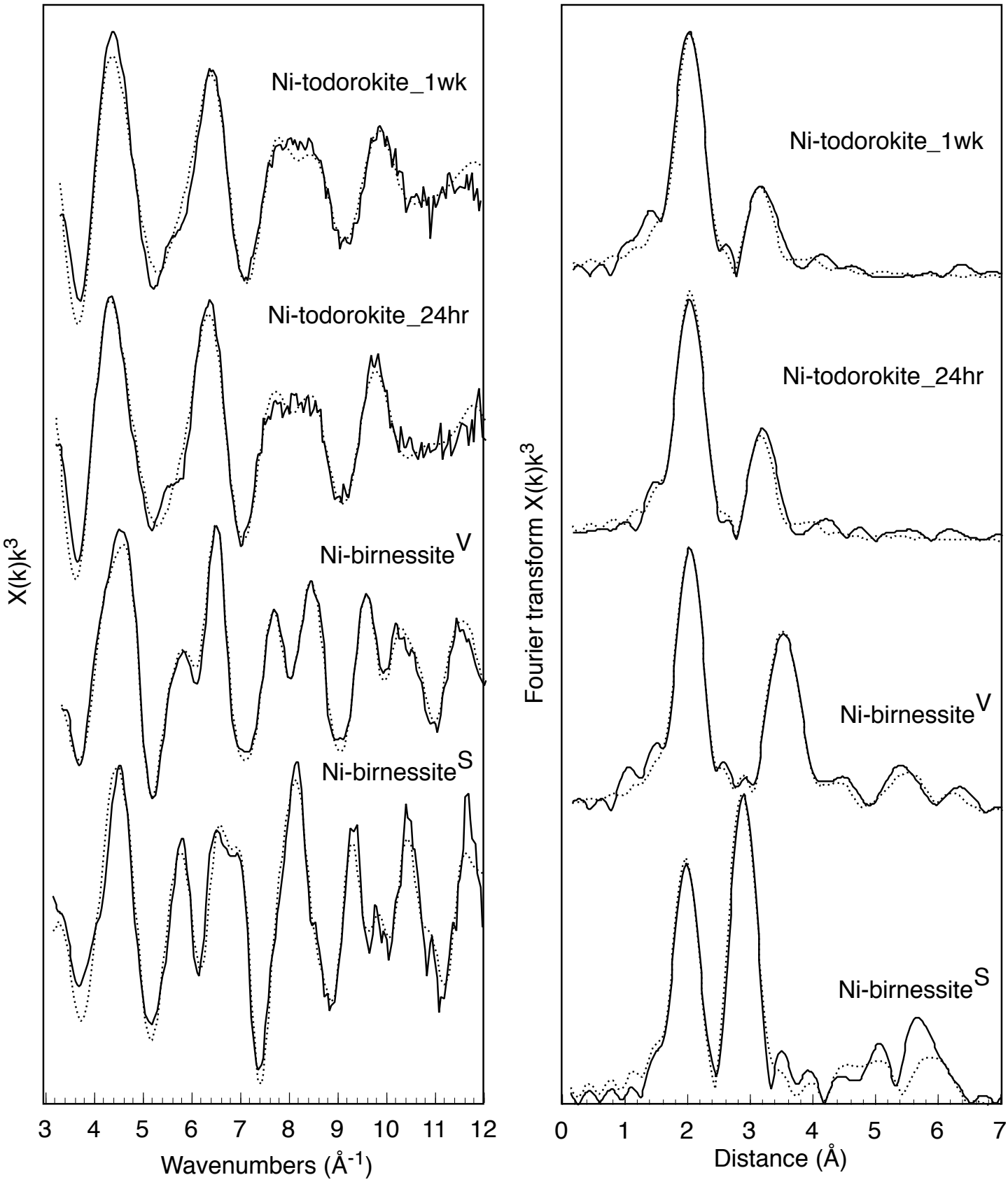

Atkins et al: Figure 6 (two columns wide)

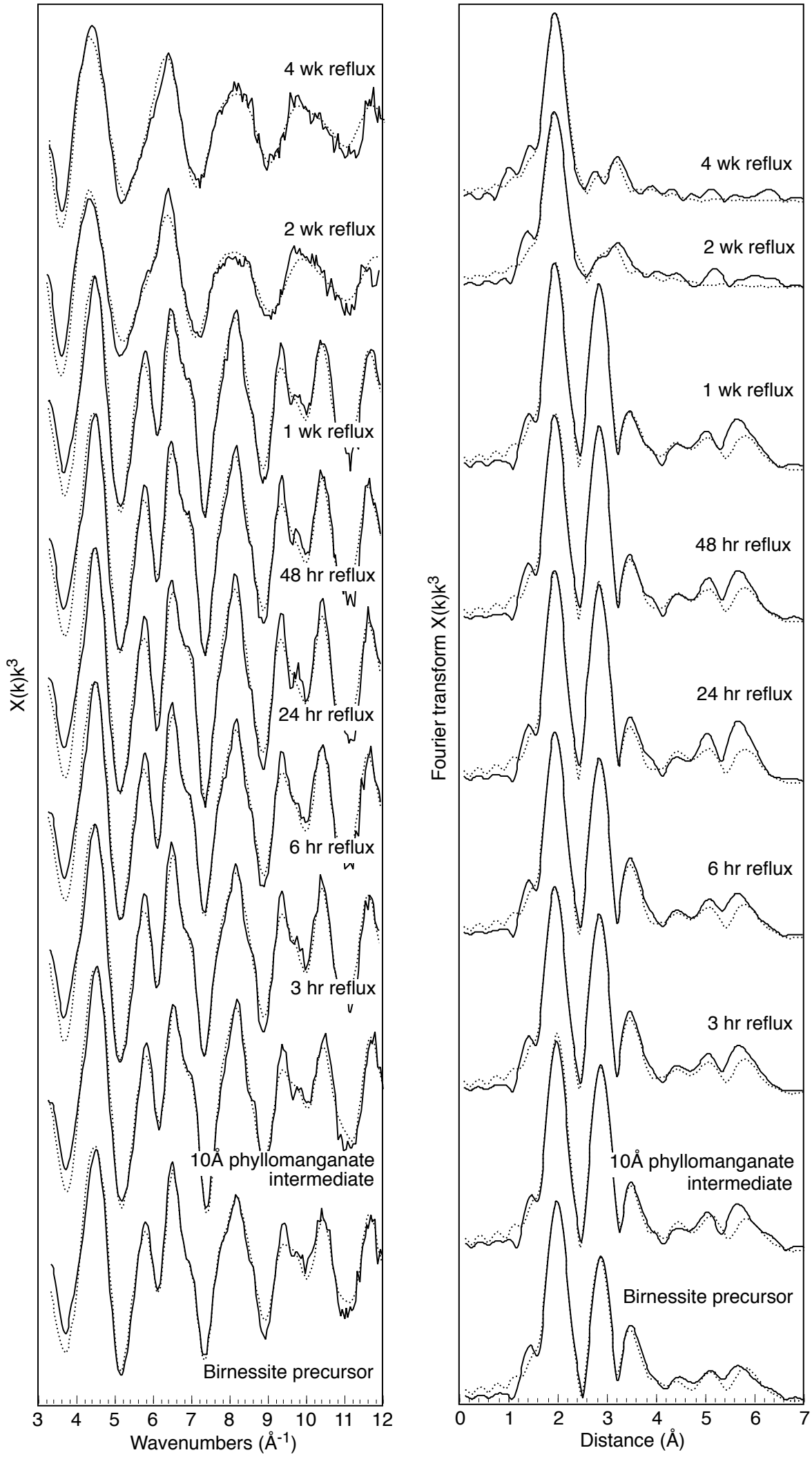

Figure7
Atkins et al: Figure 7 (one column wide)

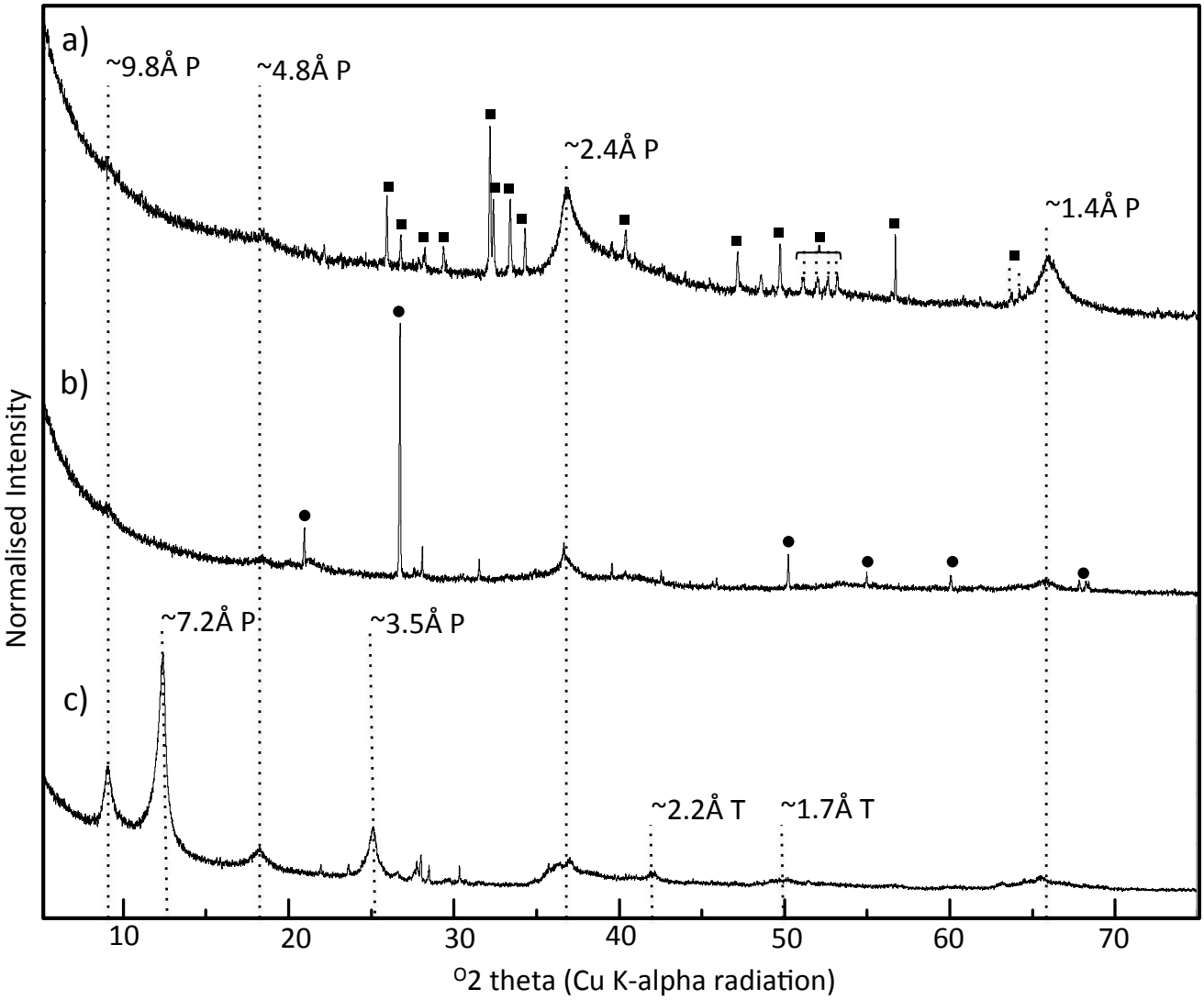

Figure8

Atkins et al: Figure 8 (two columns wide)

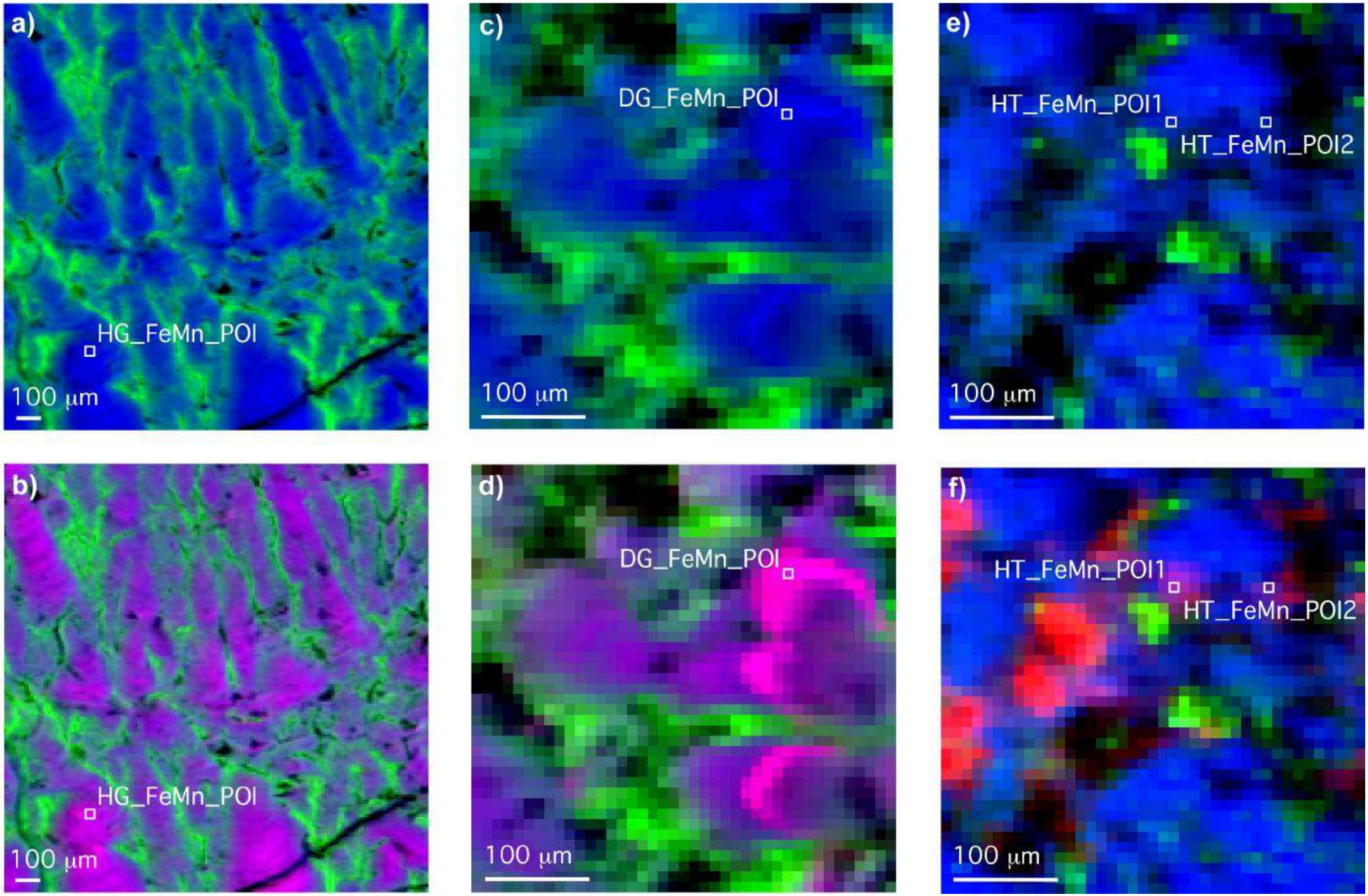

Figure9
Atkins et al: Figure 9 (two columns wide)

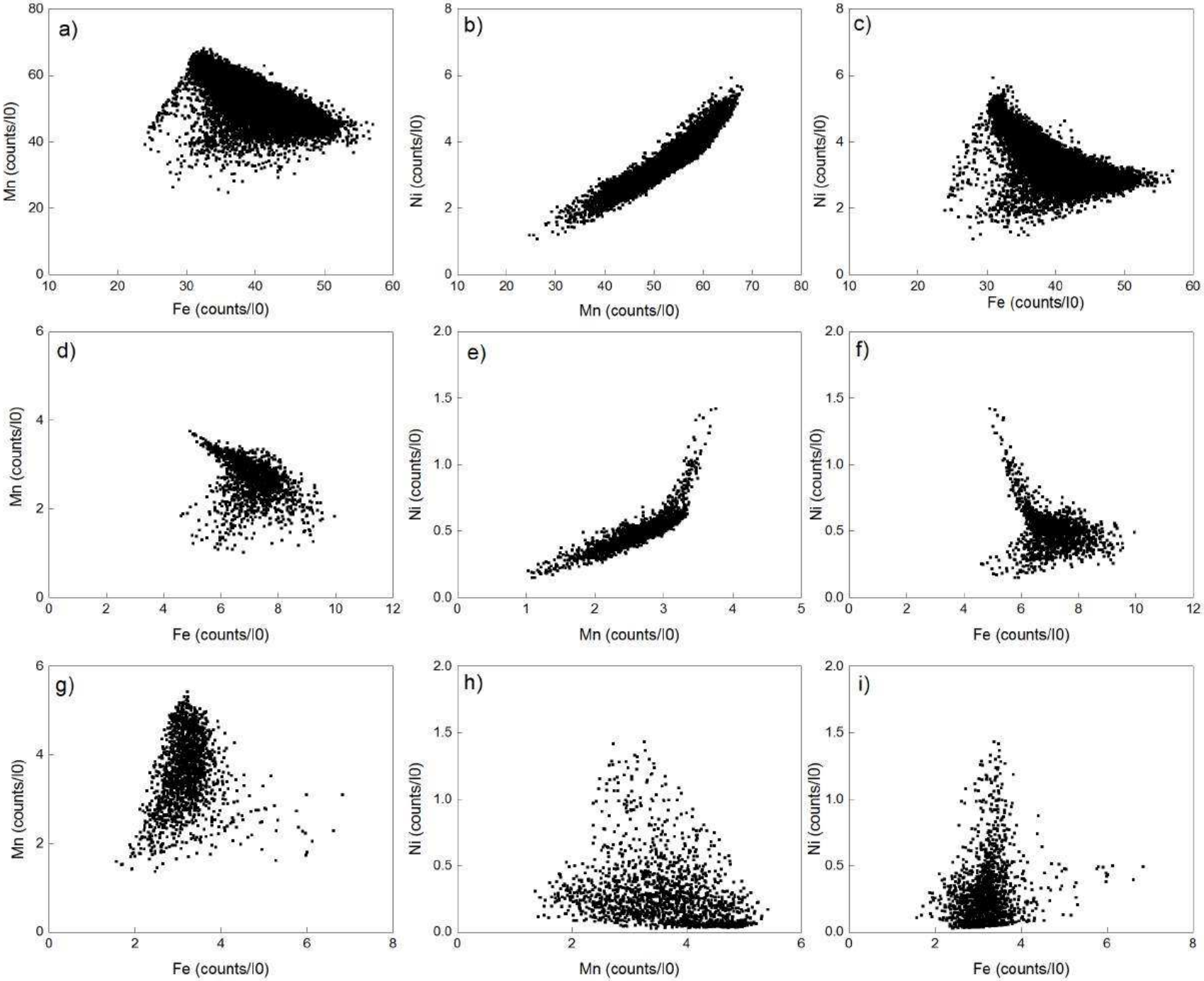

Figure10
Atkins et al: Figure 10 (two columns wide)

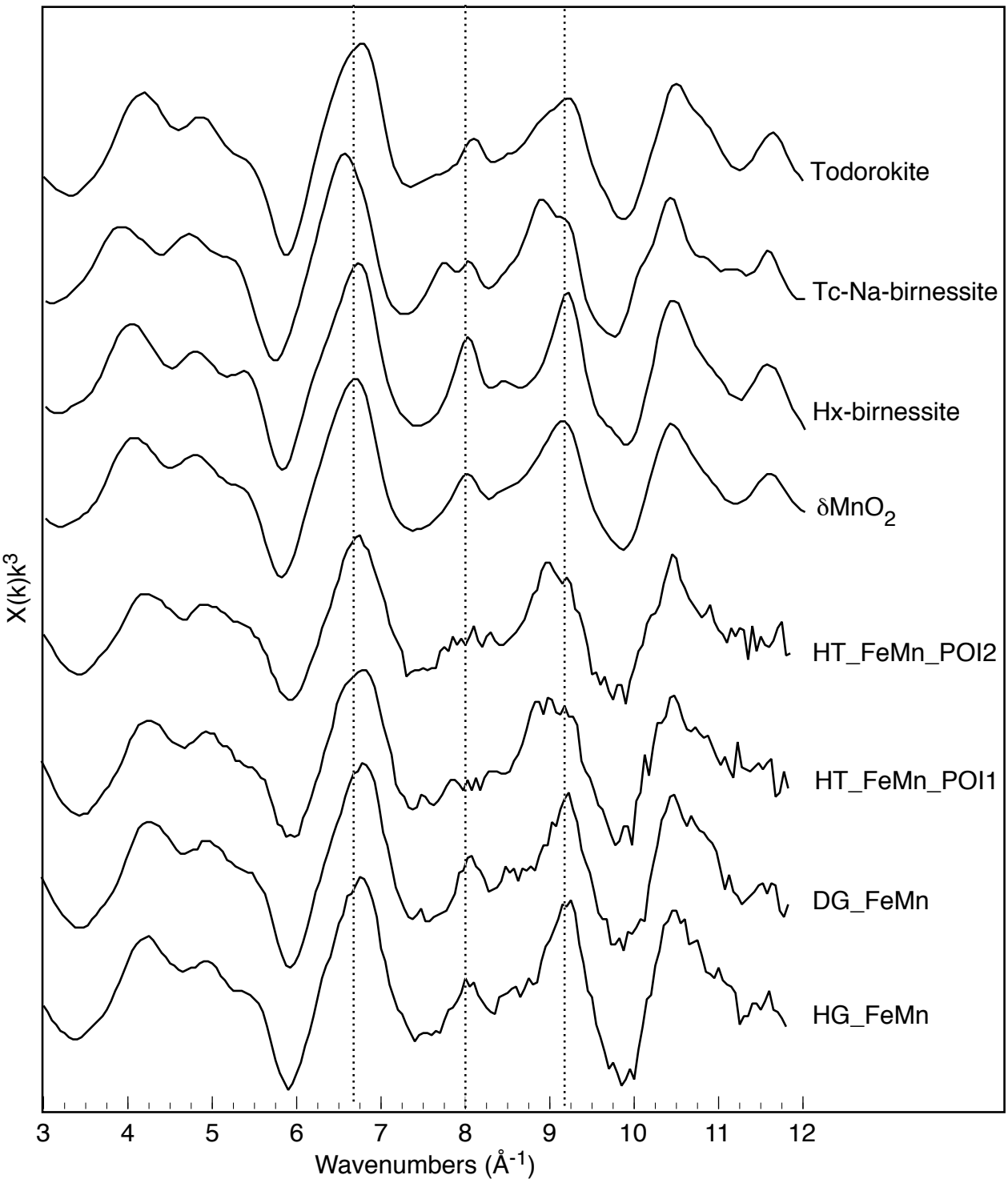

Atkins et al: Figure 11 (two columns wide)